ORIGINAL ARTICLE

Investigation of the hydrodynamic and thermodynamic behavior of the liquid jet quenching process

Nithin Mohan Narayan[1,2] · Udo Fritsching[1,2,3]

Abstract

Liquid jet quenching of metals is typically adopted to achieve specific material properties of metals, thereby making them suitable for advanced engineering applications. In this process, a metal plate is heated and cooled rapidly by impinging water jets. The temperature history during cooling leads to a microstructural transformation thereby improving the material properties such as hardness. During liquid jet quenching, since the plate surface temperature is above the Leidenfrost temperature, the boiling heat transfer dominates. This is associated with an intense cooling and water vapor generation, where the Leidenfrost effect impedes the immediate wetting of the surface. The resulting uneven cooling over the plate surface tends to potential deformation and cracking. To control this process, a detailed understanding of the spatial and the temporal heat transfer behavior is imperative. Experiments in this context are limited and therefore investigating the conjugate heat transfer process is to be combined with a multi-phase numerical model. The two-phase numerical model based on the Euler-Euler approach is developed and validated to simulate the jet quenching of a stationary plate considering all the boiling regimes within a single framework. This model consists of two phases, the liquid water which is the continuous phase (primary) and the water vapor modeled as the dispersed phase (secondary). In this study, a circular water jet (tap water) impact is considered and the plate materials under investigation are aluminum alloy (Al-alloy) and stainless steel (St-steel). Experiments are performed using infrared and high-speed imaging. The validated numerical model provides the technical parameters such as wetting front behavior, heat flux, HTC (heat transfer coefficient) etc. The influence of the jet Reynolds number and the plate material properties on the heat transfer is analysed. The study emphasizes that the plate material has a significantly higher influence on the heat transfer during jet quenching.

Keywords Water jet quenching · Boiling · Leidenfrost effect · Infrared imaging · High-speed imaging · Two-phase flow · Euler-Euler numerical model · Bubble crowd boiling model

Nomenclature

Al-alloy	Aluminum alloy (AA6082)
d	Diameter [mm or m]
C	Constant [-]
C_p	Specific heat capacity [J/(kg·K)]
DNB	Departure from nucleate boiling
exp	Experiment
f	Function
fps	Frames per second
g	Gravity [m/s²]
h	Total enthalpy [J]
h_{film}	Water film height [mm or m]
h_v	Latent heat of evaporation [J/kg]
H	Distance between surface and nozzle [mm or m]
HF	Heat flux [W/m² or MW/m²]
HLRN	North-German Supercomputing Alliance
HTC	Heat transfer coefficient [W/(m²·K) or kW/(m²·K)]
IR	Infrared
m	Phase liquid or vapor
$\dot{m}$	Mass flow [kg/s]

Highlights

"Investigation of the hydrodynamic and thermodynamic behavior of the liquid jet quenching process"

- Numerical modeling and simulation for the quenching of a stationary metal plate with a single circular (full) jet including boiling and conjugate heat transfer.
- Experiments with infrared and high-speed imaging for validating the numerical model.
- Computing the transient heat flux, heat transfer coefficient, Leidenfrost temperature, wetting front radius etc.
- Influence of the jet Reynolds number and the plate materials on heat transfer analysed numerically.

Extended author information available on the last page of the article

n	Power factor
NHR	National high performance computing
p	Pressure [Pa]
px	Pixel
$\dot{q}$	Heat flux [W/m^2]
r	Radial distance from jet axis [mm or m]
R	Wetting front radius [mm or m]
R^2	Coefficient of determination [-]
Re	Reynolds number [-]
simu	Simulation
S	Source or sink term
St-steel	Stainless steel 1.4828
SF	Nucleation suppression factor
t	Time [s]
t_o	Jet contact instant with the hot plate
T	Temperature [K or ℃]
T_p	Plate temperature in furnace [K or ℃]
$T_{p,o}$	Plate temperature at start of quenching [K or ℃]
u	Velocity vector [m/s]
UDF	User defined function
U-R	Under relaxation [-]
V	Velocity [m/s]
w	Width [mm or m]
y+	Non-dimensionless distance [-]
2D	Two dimensional
3D	Three dimensional
ε	Emissivity [-]
ρ	Density [kg/m^3]
μ	Viscosity [Pa·s]
α	Volume fraction [-]
τ	Stress tensor [N/m^2]
Δt	Time step [s]

Subscripts

boi	Boiling
con	Convective
crit	Critical
exp_average	Average from experiments
f	Fluid
f_film	Fluid film
f_film_avg	Average along fluid film height
i	Vector index
imp	Impinging
j	Vector index
leid	Leidenfrost
l	Liquid
max	Maximum

max_Tf	Maximum based on constant fluid temperature
max_Tboi	Maximum based on boiling temperature
max_Tf_film_avg	Maximum based on fluid film average temperature along height
max_Twater	Maximum based on constant water temperature
max_Twater_film_avg	Maximum based on water film average temperature along the film height
MHF	Maximum heat flux
nb	Nucleate boiling
non_imp	Non-impinging surface
pc	Precooling
s	Surface
simu	Simulation
sat	Saturation
v	Vapor
wf	Wetting front
95%Tp,o	95% of initial plate temperature

1 Introduction

During the heat treatment stages in the metal industries such as hot rolling, continuous casting etc., the liquid jet or spray quenching is introduced to improve specific material attributes [1, 2]. The metal plates are intensively heated to high temperatures and subsequently quenched with liquid jets or sprays. The resulting spatial and temporal heat transfer behavior determines the final quality of the product such as hardness. As the plate surface temperature is above the Leidenfrost temperature, the heat transfer is dominated by boiling with intense vapor generation. The challenge of the process is to establish a specific wetting action across the plate surface. Due to the Leidenfrost effect, an uneven cooling process may arise. This can result in residual thermal stresses that cause material deformation and cracking by which the cost of production is unnecessarily increased. A thorough understanding of the spatial and temporal evolution of the heat transfer during quenching is essential to achieve an energy efficient quenching process with minimum material damage.

Full (circular) jet, flat jet and spray nozzles are generally preferred for the liquid quenching in which the full jet providing an intensive cooling of surface and spray nozzle exhibiting moderate or lower quenching intensity. The wetting front behavior for the three different nozzle types discussed above is depicted in Fig. 1(a–c) during the quenching of a 2 mm thick stainless-steel sheet with a surface temperature above the Leidenfrost temperature. The full jet has
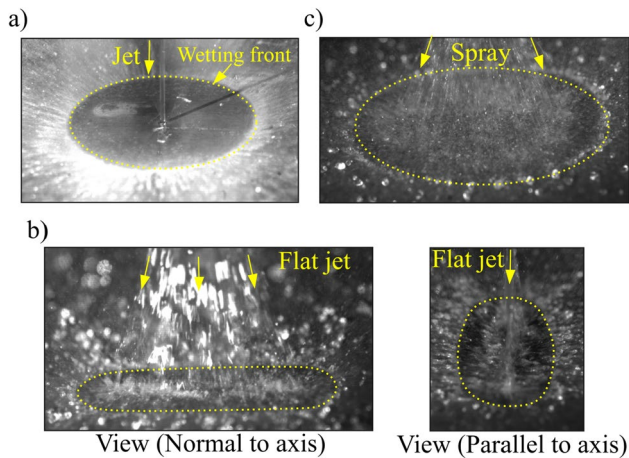
Fig. 1 Wetting front for **a** full jet quenching **b** flat jet quenching **c** full cone spray quenching with a surface temperature above Leidenfrost temperature

a circular wetting front that spreads radially outwards with time (Fig. 1a), while the flat jet possesses a wetting front that propagates both along the axis direction and perpendicular to the axis (Fig. 1b). A full cone spray has a circular wetting front which is highly transient as seen in Fig. 1c. In these cases, the inner region (dark zone) is wetted and the outer region is non-wetted.

This study focuses on the full jet quenching with water for a stationary plate. The full jet behavior at different jet velocities (V_{jet}) during impingement on a cold plate is shown in Fig. 2(a–c) where a hydraulic jump can be observed. At lower velocities, a smooth liquid film as well as transition to the hydraulic jump is observed. However, as the jet velocity V_{jet} (jet Reynolds number/Re_{jet}) increases, the water film is strongly disturbed by surface waves and turbulence. In [3], it has been observed that an increased Re_{jet} can upsurge the
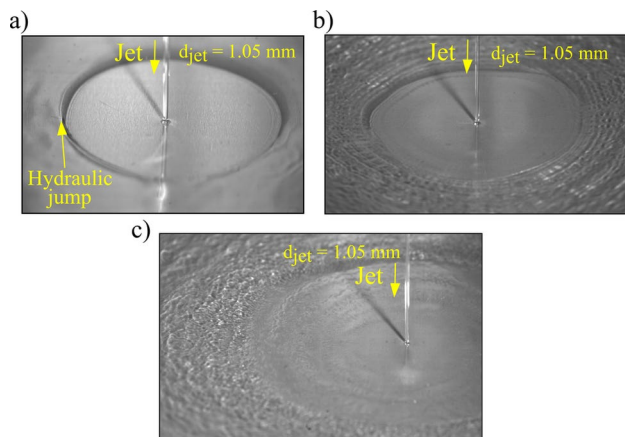

Fig. 2 Full jet ($d_{jet} = 1.05$ mm) behavior during impingement over a cold plate **a** $V_{jet} = 10.3$ m/s ($Re_{jet} = 10773$) **b** $V_{jet} = 13.3$ m/s ($Re_{jet} = 13912$) **c** $V_{jet} = 18$ m/s ($Re_{jet} = 18828$)

splattering mass from the liquid film. This study focuses on quenching in areas where the radius is smaller than the hydraulic jump radius. Thus, the hydraulic jump effects are not considered here.

During the jet quenching process, the boiling heat transfer regimes such as film boiling, transient boiling, nucleate boiling and convective cooling occur simultaneously over the quenched surface. Different boiling regimes are shown schematically in Fig. 3 for a single full jet quenching. At higher surface temperature (T_s) vapor bubble crowds together and film boiling occurs (region 1) with poor heat transfer characteristic. As the surface temperature $T_s < T_{leid}$, a wetting is initiated, thereby entering into region 2,3, where the transient and nucleate boiling takes place with an increased heat transfer rate. This is followed by region 4, which is a convective cooling without any vapor generation. The local heat transfer rate at the plate surface is contingent on the active boiling regime.

The analysis of this process by experiment alone suffers from technical limitations and the complexity of the process. In addition, the technical parameters such as heat flux, HTC etc., of the impinging surface cannot be obtained directly from an experiment. Inverse calculations of surface temperature are mostly preferred to derive the heat flux, HTC etc., which are based on the plate backside (non-impinging) temperature measurements. Therefore, a numerical model is desirable to investigate the temporal and spatial heat transfer during this conjugate heat transfer process. In addition, the results obtained from the numerical models can further assist in the process optimization and plant design [4–7].

Most of the previous studies investigated the jet quenching process by experimental investigation and inverse analysis [8–14]. Only limited work is currently available on the numerical modeling of the liquid jet quenching, where most works mainly focuses on a single boiling regime [15, 16]. The bubble crowd boiling model which is basically developed in a 2D domain [17–20] can simulate the boiling flow considering all the boiling regimes with a single framework. In this model, the vapor bubble diameter is input parameter as a linear function of the local vapor volume fraction, but the Leidenfrost temperature is not required as an input
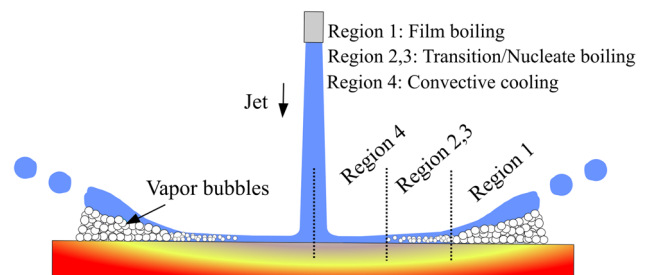
Fig. 3 Schematic of the boiling regimes during full jet quenching

parameter. Recent work [21] simulated the quenching of a metal specimen in water considering all the boiling regimes. Here, the Leidenfrost temperature and the vapor bubble diameter were given as inputs.

There is an increasing demand for jet quenching simulations involving multiple jets, pulsating jets and moving plates [4]. To realize this, a fully functional and validated two-phase numerical model in the 3D domain is necessary. Therefore, the bubble crowd boiling model [17–20] has been adopted in this work and extended to simulate the quenching of a single water jet in the 3D domain with a stationary plate. This model is based on the Euler-Euler framework and consist of two phases. The liquid water acts as a continuous phase and the water vapor as a dispersed phase.

Experiments are carried out to analyse the hydrodynamic and thermodynamic behavior of a single water jet quenching process using infrared and high-speed imaging techniques and to validate the numerical model. High-speed imaging is intended to observe the wetting front evolution during quenching and infrared imaging is performed to measure the temperature at the non-impinging plate surface (back side). In order to have a valid numerical model, the validation is carried out at two different plate materials, one with a lower thermal conductivity and another with a higher thermal conductivity as well as for two different initial plate temperatures. The validated numerical model can provide the important hydrodynamic and thermodynamic parameters such as wetting front behavior, heat flux, HTC, cooling curve etc. The influence of the jet Reynolds number and plate materials on the heat transfer nature is numerically investigated based on the validated model.
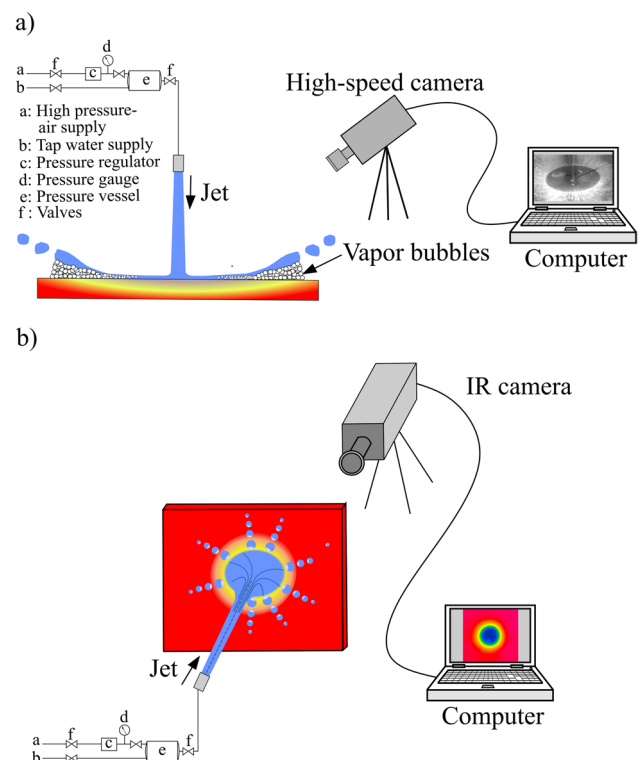
2 Materials for investigation

Two industrially relevant plate materials such as aluminum alloy (AA6082) and stainless-steel (1.4828) are selected as investigating materials. The material properties of the Al-alloy are adopted from [4] and that of the St-steel from [22] as summarised in Table 1. To evaluate the versatility of the developed numerical model, the investigation with a higher and a lower thermally conductive plate material is scheduled. The quenching fluid is tap water.

Table 1 Properties of plate materials under investigation [4, 22]

Property with SI Unit	Al-alloy (AA6082)	St-steel (1.4828)
Density [kg/m^3]	2700	7900
Specific heat capacity [J/(kg·K)]	998	528.3
Thermal conductivity [W/(m·K)]	200	16.6

3 Experimental setup

Two experimental configurations are set up as illustrated in Fig. 4. The first configuration Fig. 4a (vertical jet) is used to analyse the wetting front propagation with high-speed imaging and with the second configuration Fig. 4b (horizontal jet), the surface temperature measurement with the infrared imaging is performed. High-speed imaging is performed using a FASTCAM SA4 Photron camera with a frame rate of 1000 fps and a suitable lighting system (Dedolight DLH400D). Infrared imaging is carried out with the camera ImageIR 8300 [23] where the measurements are executed at a frequency of 10 Hz. The metal plates have a dimension of $200 \times 200 \times 5$ mm^3. The non-impinging surface of the metal plates is coated with a black spray paint (Ulfalux [24]) to have a constant emissivity ($\varepsilon \approx 1$) during temperature measurement and is well dried before the experiment. The metal plate is heated in a furnace (THERMCONCEPT KM 50/13 [25]) to a temperature higher (T_p) than the desired temperature ($T_{p,o}$) to compensate for the heat loss during the transfer from the furnace to the test site. The Al-alloy is therefore heated to $T_p = 778.15$ K (505 ℃) and the St-steel to $T_p = 1073.15$ K (800 ℃). Sufficient furnace hold time is provided to distribute the heat evenly within the plate. The full jet nozzle (Lechler, 544.360 [26])

a)

a: High pressure-air supply
b: Tap water supply
c: Pressure regulator
d: Pressure gauge
e: Pressure vessel
f: Valves

High-speed camera

Jet

Vapor bubbles   Computer

b)

IR camera

Jet

Computer

Fig. 4 Schematic diagram of the experimental setup **a** High-speed imaging **b** Infrared imaging

with a diameter $d_{jet} = 1.05$ mm is used in experiments and the distance between the nozzle and the hot plate is maintained at H = 85 mm. The flow rate of the water jet is set constant (with constant pressure of 5 bar) which provides a jet velocity $V_{jet} = 17.7$ m/s. The water temperature measured with a K type thermocouple is 292.15 K (19 °C).

To perform the high-speed imaging, the water jet is turned on first and initially directed to a bypass for generating a developed water jet. The hot plate is then removed from the furnace and placed at the test site. The bypass is removed so that the fully developed water jet impinges at the center of the hot plate. At the same time, the high-speed camera records this process which is later post-processed with the ImageJ [27] to derive the wetting front radius over time. A vertical jet is considered in high speed imaging to better capture the process without obstruction.

The infrared camera measures the surface temperature at the non-impinging surface of the metal plate with the appropriate calibration which is post-processed with the IRBIS Professional software [28] to derive the required temperature data. The exact moment when the water jet impinges on the hot surface (t = 0 s) is determined by the movement of the bypass plate. A horizontal jet is chosen for the temperature measurement considering the feasibility of the experimental set up.

The plate surface temperature at which the water jet impinges on to the hot surface for Al-alloy is measured to be $T_{p,o} = 673.15$ K (400 °C) and for St-Steel is $T_{p,o} = 903.15$ K (630 °C). The process parameters for the validation experiments with Al-alloy and St-steel are summarised in Table 2.

4 Theoretical background

4.1 Boiling regimes

During full jet quenching of a hot surface above the Leidenfrost temperature (T_{leid}), the boiling heat transfer dominates over the surface. The region at which the surface temperature falls below T_{leid} will be wetted and the region above T_{leid} remains non-wetted. There will be higher temperature gradients across this wetted and non-wetted region, leading to material deformation and cracking. The different boiling

Table 2 Process parameters for the validation cases

Parameter	Al-alloy	St-steel
T_p	778.15 K (505 °C)	1073.15 K (800 °C)
$T_{p,o}$	673.15 K (400 °C)	903.15 K (630 °C)
T_{water}	292.15 K (19 °C)	292.15 K (19 °C)
V_{jet}	17.7 m/s	17.7 m/s
d_{jet}	1.05 mm	1.05 mm
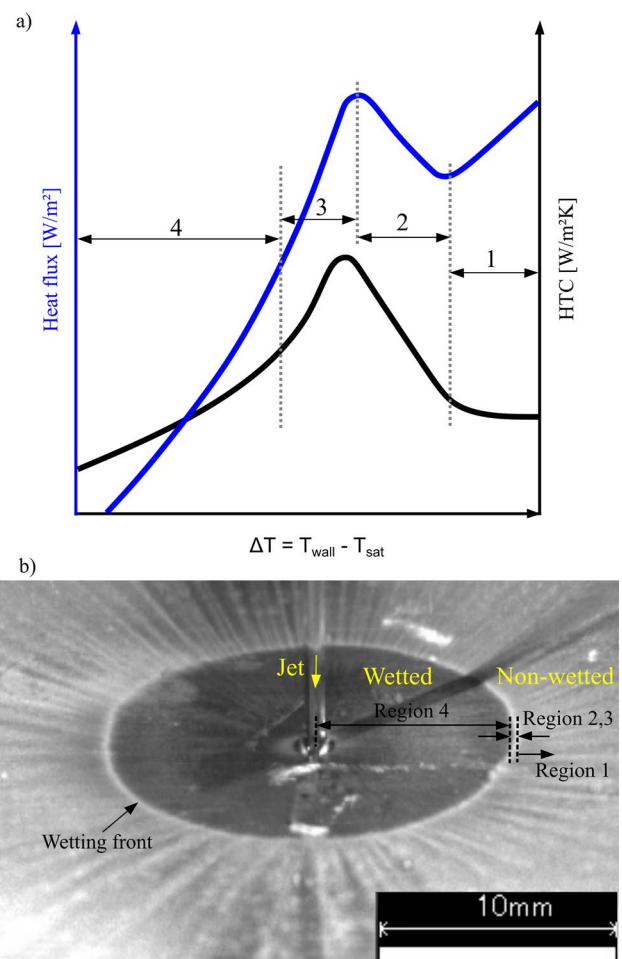
Fig. 5 **a** Nukiyama curve for water at 1 atm when started at $T_s \gg T_{leid}$ adopted from [22], **b** Boiling regimes and wetting front for jet quenching

regimes during liquid jet quenching can be described by means of the Nukiyama curve and Fig. 5a shows the boiling curve for water at 1 atm adopted from [22].

The process mainly traverses through the four heat transfer regimes film boiling (1), transition boiling (2), nucleate boiling (3) and pure convective cooling (4) which may occur simultaneously over the surface as presented in Fig. 5b for the jet quenching. Due to the higher surface temperature, a quenching process initiates from right to left (1-2-3-4). At very high temperature ($T_s > T_{leid}$), the vapor forms a vapor layer between the liquid water and the hot surface. In this regime, the heat transfer is due to conduction (and radiation) through the vapor film, where a poor heat transfer rate is observed. Once the surface temperature drops below the T_{leid}, the vapor film collapses and a partial surface wetting is initiated switching to the transient boiling regime. Here the wetted and non-wetted surfaces co-exist and the heat transfer increases approaching a maximum heat flux. This corresponds to the DNB

(Departure from Nucleate boiling) point and it is defined as the maximum heat flux point (HF_{max}) and the corresponding temperature is the maximum heat flux temperature (T_{MHF}). Thereafter, the process proceeds to the nucleate boiling regime. At this region, the heat flux continues to decrease and finally falls into a pure convective cooling regime at $T_s < T_{sat}$. The temperature decreases and there is no vapor generation.

4.2 Non-dimensionless number and HTC

The **jet Reynolds number** (Re_{jet}) is defined as the ratio of the inertial forces to the viscous forces [29]. The reference dimension is taken as the jet diameter (d_{jet}).

$$Re_{jet} = \frac{\rho_l \times V_{jet} \times d_{jet}}{\mu_l} \tag{1}$$

The **heat transfer coefficient** (HTC) is one of the most important parameters considering a conjugate heat transfer problem. It directly describes the rate of heat transfer. HTC is influenced by several factors such as the surface temperature, fluid temperature, surface nature, material type, flow velocity etc. However, computing the HTC for flow boiling is a complex process [22, 30] and has to be derived for each configuration. In this work, the maximum heat transfer coefficient (HTC_{max}) is focused and analysed, which is at the changeover from the transition to the nucleate boiling regime. At this region, the convective and the nucleate boiling heat transfer regimes are active, where the fluid and vapor bubbles co-exist near the hot surface. Measuring the fluid and the vapor temperature near the wall during quenching is not possible. In some experimental work, the HTC_f is computed by applying the HTC equation (Eq. 2) where a constant local fluid (water) temperature (T_f) is considered as the temperature of liquid jet, T_s the surface temperature and $\dot{q}$ the surface heat flux. It is also challenging to divide the heat flux based on the convective and nucleate boiling contribution at the surface.

$$HTC_f = \frac{\dot{q}}{T_s - T_f} \tag{2}$$

In the Nukiyama curve, the HTC_{boi} (Eq. 3) for pool boiling is defined in terms of the boiling temperature (T_{boi}) [31], as the water temperature has been maintained close to the boiling temperature by external heating in experiments. But in jet quenching the fluid film temperature may not reach the boiling temperature completely.

$$HTC_{boi} = \frac{\dot{q}}{T_s - T_{boi}} \tag{3}$$

During jet quenching, the wetting front propagates along the hot surface. This implies that the viscous and thermal boundary layers are not fully developed. At this stage, the fluid temperature will increase in radial direction. Simultaneously the liquid temperature decreases in wall normal direction away from the hot surface towards the fluid film surface obtaining a complex scenario i.e. $T_{f\_film} = f(r, h_{film})$ as a function of the radial distance and the fluid film height. Different approaches for computing the HTC for the two phase flow are discussed in Refs. [30, 32]. The approach of Gungor and Winterton [33] for the nucleate boiling regime is described in Eq. 4, where SF is the nucleation suppression factor. Here, the overall heat flux is equated to the convective and nucleate boiling where separate HTC are calculated. However, determining the local fluid temperature (from the fluid vapor mixture) at the hot surface is complex. As this is not even obtained directly from a two-phase simulation. Thus, the simulation may provide an overall heat flux but the ratio of the convective and the nucleate heat flux or HTC is not known.

$$\dot{q} = HTC_{con}(T_s - T_f) + SF \times HTC_{nb}(T_s - T_{boi}) \tag{4}$$

To overcome this problem and to have a more realistic HTC, an average fluid film temperature ($T_{f\_film\_avg}$) is computed in this work at the maximum heat flux point, where the average film temperature is calculated along the fluid film height (h_{film}). Equation 4 is rewritten considering $T_{f\_film\_avg} = T_{boi} = T_f$. Thereby, $HTC_{f\_film\_avg}$ is based on an average fluid film temperature as simplified in Eq. 5 which is expected to give a more realistic HTC from the computed heat flux ($\dot{q}$).

$$HTC_{f\_film\_avg} = \frac{\dot{q}}{T_s - T_{f\_film\_avg}} \tag{5}$$

The overall heat flux is fundamentally analysed in this study and the maximum HTC_{max_Tf} based on constant fluid temperature, the maximum HTC_{max_Tboi} based on the boiling temperature and the maximum $HTC_{max\_Tf\_film\_avg}$ based on the average fluid film temperature along the fluid film height at the maximum heat flux point are compared.

For typical two-phase boiling flows, the HTC can also be described as a power law with a constant and heat flux [30, 34] as shown in Eq. 6.

$$HTC = C \times (\dot{q})^n \tag{6}$$

5 Assumptions for this study

The numerical model is developed by assuming a two-phase simulation with liquid water and water vapor. However, in reality, this process involves a three-phase flow with liquid

water, vapor and atmospheric air. This assumption helps to reduce the model complexity and the number of equations to be solved thereby reducing the computational effort.

The surface of the hot plate is assumed to be smooth and surface roughness is not considered in this analysis. A rough surface may slow down the propagation of the wetting front [14].

In the developed model, the radiative heat transfer is not taken into account because the initial temperature is not high enough and the duration of the process is short.

The distance between the nozzle and the hot plate (H) in the experiment is 85 mm (to include the bypass), but in the simulation, it is considered smaller as H = 20 mm, which significantly reduces the size of the computational domain and the computational effort, without significantly affecting the results.

A horizontal jet and a vertical jet will give similar results for the time duration considered in this study t < 0–3.5 s which will be verified in Section 6.2. Therefore, all the simulations are modeled in a vertical jet configuration in order to avoid highly transient vapor motions, which also helps to reduce the computational effort.

6 Experimental analysis

6.1 Wetting front behavior from high-speed imaging

Figure 6 illustrates the initial time instants during the water jet impingement on a 5 mm Al-alloy plate with $T_{p,o} = 673.15$ K. It has been observed that the water jet impact does not cause an immediate wetting on the hot

Fig. 7 Wetting front propagation for 5 mm Al-alloy quenching with $d_{jet} = 1.05$ mm, $V_{jet} = 17.7$ m/s ($Re_{jet} = 18514$) and $T_{p,o} = 673.15$ K (validation case)

surface due to the Leidenfrost effect. During t < 25 ms, the water flows over the surface without making any actual wetting. After a certain time the wetting is initiated and propagates radially outwards, which can be distinguished by a dark zone up to the water film lift off. For Al-alloy, the wetting initiation delay resides in the range $t_{delay} = 15$–30 ms. Similar wetting initiation delay has been observed for St-steel quenching in [18].

The wetting front propagation (R_{wf}) for the Al-alloy (validation case) quenching is presented in Fig. 7. After wetting is established, the wetting front propagates radially outwards. A water film ejection is noticeable at the periphery where the water film is lifted from the hot surface due to vapor film formation and the Leidenfrost effect. The wetting front radius (R_{wf}) is observed to increase with time.

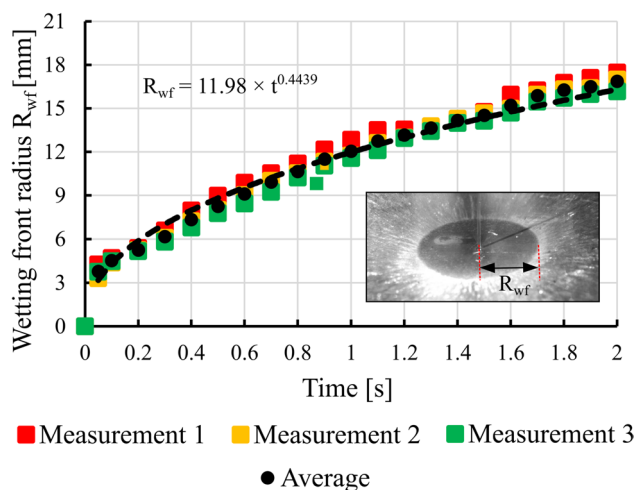The evolution of the wetting front radius (R_{wf}) with time for the Al-alloy quenching (validation case) for three

Fig. 6 Wetting initiation delay during 5 mm Al-Alloy plate quenching with $d_{jet} = 1.05$ mm, $V_{jet} = 17.7$ m/s and $T_{p,o} = 673.15$ K (400 ℃)

Fig. 8 Wetting front radius (R_{wf}) over time for the 5 mm Al-alloy quenching with $d_{jet} = 1.05$ mm, $V_{jet} = 17.7$ m/s ($Re_{jet} = 18514$) and $T_{p,o} = 673.15$ K (validation case)
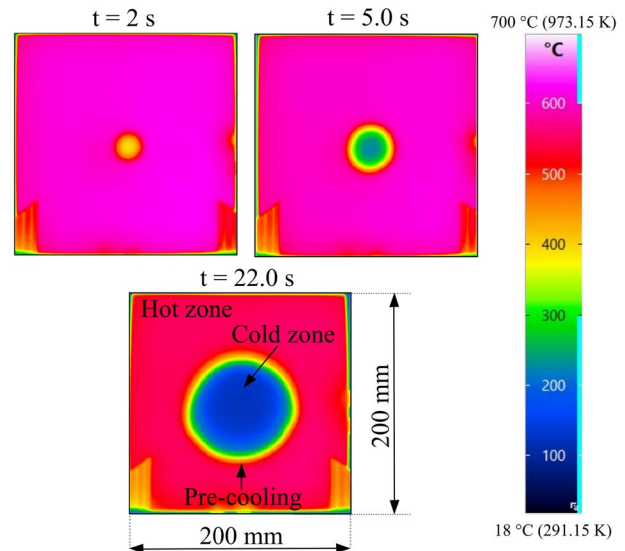
measurements is depicted in Fig. 8. The measurements are repeatable and R_{wf} increases with time. At the beginning, the curve has a higher slope which decreases in course of time. This means that the wetting front propagation decelerates with time. This is due to the fact that the fluid film velocity declines over the radius during radial film propagation. The behavior of R_{wf} can be quantitatively represented by a power law (Eq. 7) for the Al-alloy quenching (validation case) with $V_{jet} = 17.7$ m/s and $T_{p,o} = 673.15$ K.

$$R_{wf} = 11.98 \times t^{0.4439} \text{ with } R^2 = 0.98 \tag{7}$$

6.2 Temperature contours from infrared imaging

The temperature contours at the non-impinging surface (plate backside) for the Al-alloy quenching (validation case) are shown in Fig. 9. The inner cold zone enlarges with time which is similar to the wetting front propagation observed earlier. Just outside the cold zone a precooling of the surface towards the hot zone can be observed. The precooling effect towards the hot zone increases with time. This is due to the thermal conduction in the plate.
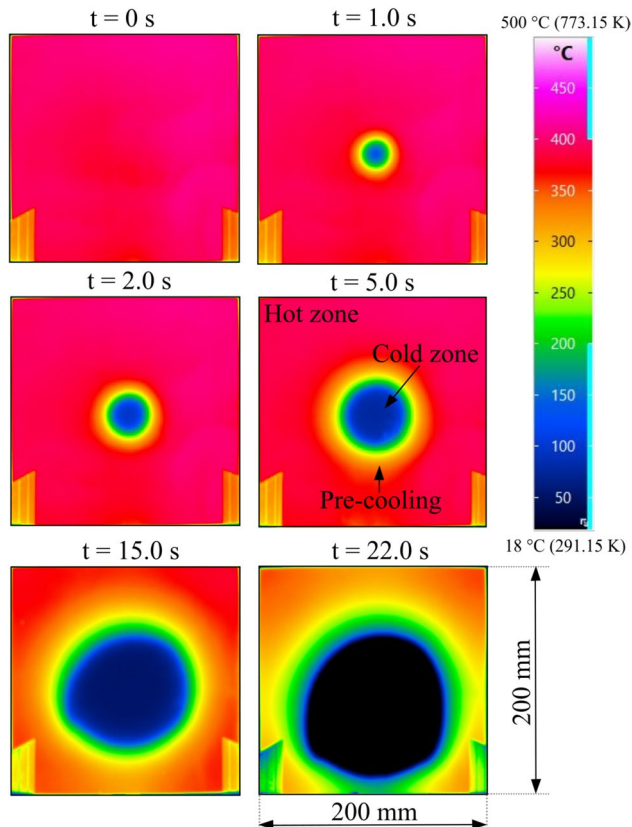
Furthermore, even with a horizontal jet quenching (vertical plate) the cold zone is symmetrical up to t = 5 s. Asymmetrical behavior can be noticed only at a later stage such as time instants t = 15 and 22 s.

The non-impinging surface temperature at different time instants for St-steel quenching (validation case) is shown in Fig. 10. This also shows a similar trend as in Al-alloy, the cold zone grows with time. Although, the initial temperature of the two cases are not comparable, a slower propagation of the cold zone is observed for St-steel when comparing at t = 22 s with the Al-alloy (Fig. 10). It may also be possible that a larger cold zone exists at the impinging surface and only a smaller cold zone is seen at non-impinging surface (camera side) for the St-steel due to the poor material conductivity.

A lower precooling of the surface is observed for St-steel quenching. This is because the lower thermal conductivity of the material results in higher heat transfer resistance. Moreover, it can also be seen from Figs. 9 and 10 that the overall hot zone temperature slowly decreases with time, due to the heat transfer to the surrounding and the precooling effect.

6.3 Temperature curves from the infrared analysis (non-impinging surface)

Figure 11 compares three consecutive temperature measurements (raw data) at the radial position r = 30 mm for Al-alloy quenching (validation case). The results demonstrate that the measurements are repeatable with a maximum standard deviation of 12 °C. The initial plate temperature $T_{p,o}$ for measurement 3 is lower that in the other cases, thus causing the temperature curve shift.

Fig. 9 Temperature contours at non-impinging surface during Al-alloy quenching from validation case with $d_{jet} = 1.05$ mm, $V_{jet} = 17.7$ m/s ($Re_{jet} = 18514$) and $T_{p,o} = 673.15$ K

Fig. 10 Temperature contours at non-impinging surface during St-steel plate quenching (validation case) with $d_{jet} = 1.05$ mm, $V_{jet} = 17.7$ m/s ($Re_{jet} = 18514$) and $T_{p,o} = 903.15$ K
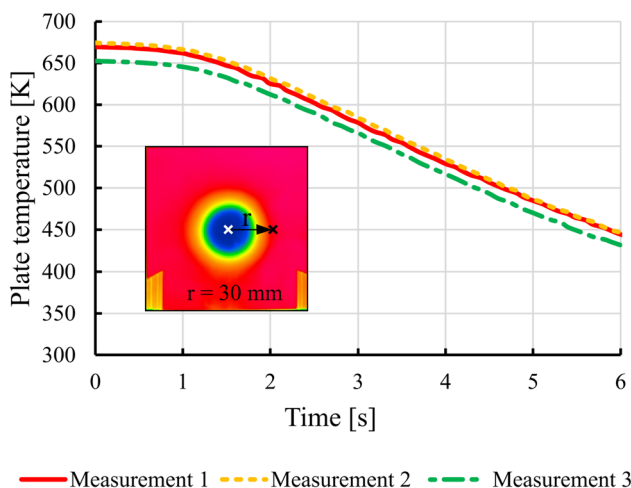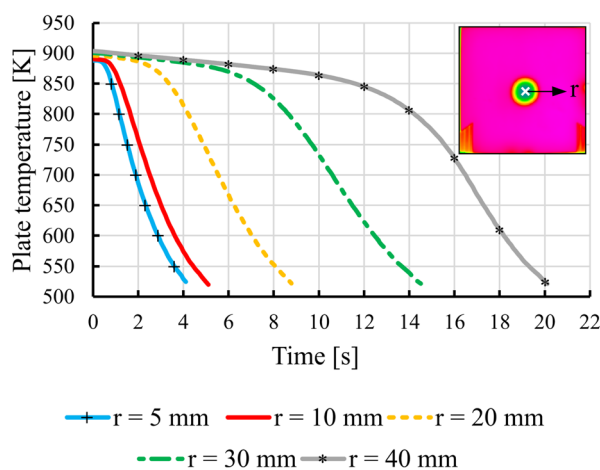
Fig. 11 Repeatability study of measurements from Al-alloy quenching (validation case), plate temperature at non-impinging surface ($r = 30$ mm)

The cooling curves for Al-alloy jet quenching (validation case) at distinct spatial positions such as $r = 10, 20, 30$ and 40 mm are depicted in Fig. 12. The raw data are smoothened using a Savitzky-Golay filter. The results show that the cooling intensity is higher close to the jet axis and decreases further downstream. This is due to the fact that the momentum and velocity close to the jet axis is higher and the film velocity decreases with time i.e., over the radial positions. The precooling effect due to conduction in the plate can be seen from the curves e.g., with the curve at $r = 40$ mm, before the arrival of the wetting front, the temperature already slowly decreases at $t = 0$–1.5 s in the hot zone.

The temperatures at the non-impinging surface for St-steel quenching (validation case) are presented in Fig. 13. The trend
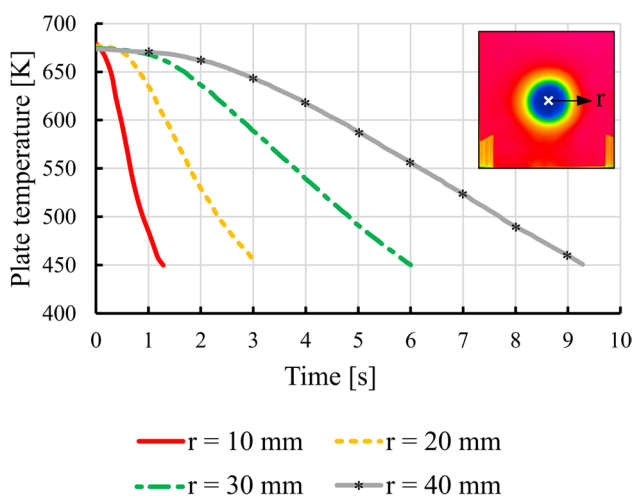
remains the same, the spatial position close to jet axis are cooled down faster. In contrast to the Al-alloy, the temperature curve does not drop quickly before the arrival of the wetting front. This means that a lower precooling can be expected in the St-steel plate due to the poor thermal conductivity.

6.4 Error sources and estimation

During the experiments with infrared and high-speed imaging, several sources of error could be encountered as well as during the data processing which are briefly discussed with their influence on the results.

The data processing with the infrared analysis is done by means of pixel distance (px) and the center of the jet impact is identified by the image analysis and as the center of the cold zone from $t = 1.0$ s. From this reference jet impingement center, the further radial positions (r) are computed. In this analysis, one px in x direction is about 0.62 mm. The identification of the jet center may have an error. Figure 14 presents the influence of pixel selection/jet center on the temperature curves. Here, the position $r = 20$ mm is shown as a reference example and the distance are varied from px = 1, 2 and 3 to the left and also to the right of the reference point. It is to be seen that the results are impacted by the px selection. An error of about 1–2 px is estimated in this work during the determination of the jet center. Moreover, the plate may deform during the quenching process and the infrared measurements does not account for this which can also influence the results since a fixed px is used for data processing. A maximum deviation in temperature up to 10–20 K can be expected.

The emissivity of the black coating applied to the plate non-impinging surface for the infrared measurements and

Fig. 12 Cooling curves at the non-impinging surface during Al-alloy quenching with $d_{jet} = 1.05$ mm, $V_{jet} = 17.7$ m/s ($Re_{jet} = 18514$) and $T_{p,o} = 673.15$ K (validation case)


Fig. 13 Cooling curves at the non-impinging side for St-steel quenching with $d_{jet} = 1.05$ mm, $V_{jet} = 17.7$ m/s ($Re_{jet} = 18514$) and $T_{p,o} = 903.15$ K (validation case)
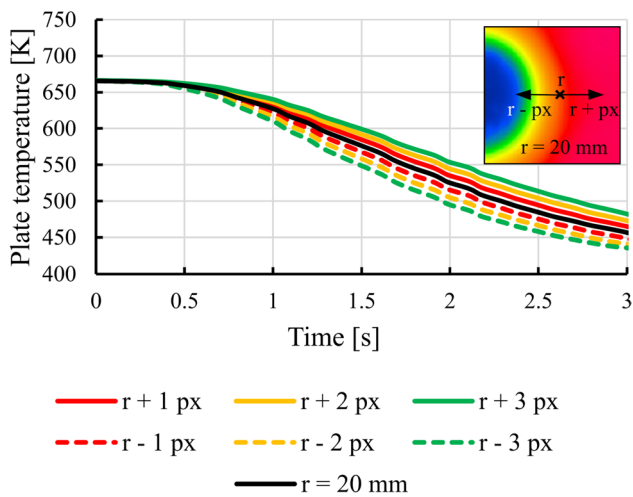
Fig. 14 Influence of pixel selection (jet center) on temperature curves from Al-alloy quenching (validation case)

data processing is considered with an ideal case with emissivity $\varepsilon = 1$. However, some studies show that this may be slightly affected by the coating [14]. In order to determine its influence on the results, the temperature curves from the Al-alloy quenching at the radial position $r = 20$ mm from the non-imping surface are derived for $0.9 < \varepsilon < 1$ as shown in Fig. 15. The results show only a minor influence on the temperature behavior. Between the temperature measurements with $\varepsilon = 1$ and 0.9 a maximum temperature difference of about 12.6 K is observed (percentage deviation of 2%). Thereby, the ideal case $\varepsilon = 1$ will not significantly impact the results and is considered in this study.

While comparing experimental results with numerical results, the synchronisation of the data on the time scale for the intensive cooling process is very important. In jet quenching experiments, the temperature measurements are
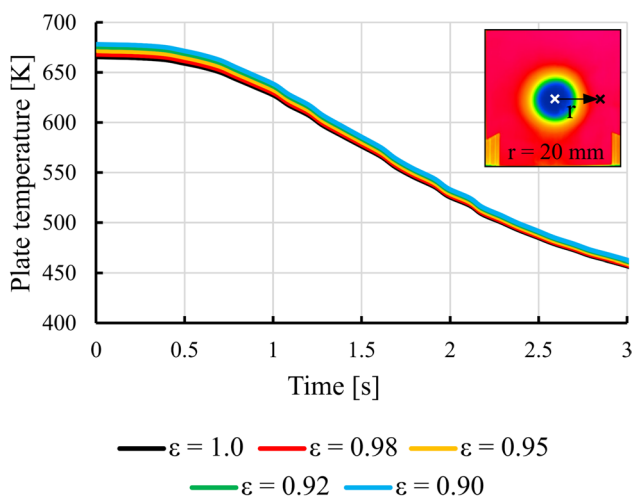
Fig. 15 Influence of emissivity on temperature curves from Al-alloy quenching (validation case)
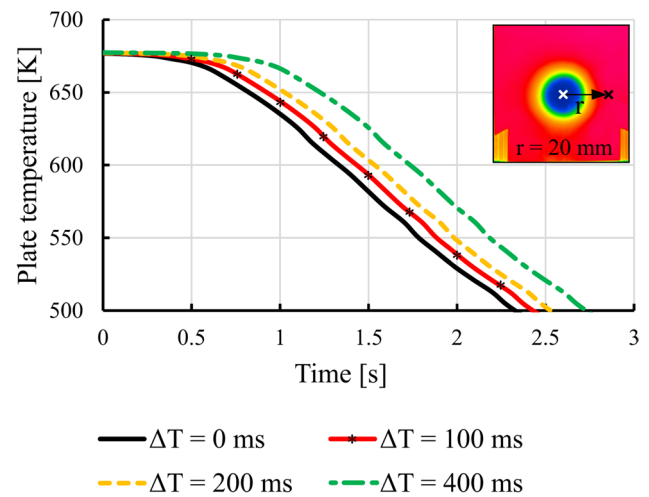
Fig. 16 Influence of determining jet impact time instant on hot plate ($t_o = 0$ s) from experiment during 5 mm Al-alloy quenching (validation case)

taken from the non-impinging surface and the quenching process occurs at the impinging surface. Especially with a thick plate, the cold zone is visible on the camera side only after a certain time $t_o + \Delta t$. Therefore, the exact jet impingement instant ($t_o = 0$ s) is required. In this work, t_o is taken from the bypass motion before the jet impingement. The influence of improper start impact identification ($t_o = 0$ s) can influence the temperature distribution and results in large synchronisation error while comparing with the numerical result. In Fig. 16 the influence of start point determination ($t_o = 0$ s) is presented assuming an error of $\Delta t = 100$, 200 and 400 ms. The results show that it can influence the temperature curve to a greater extent. In this work, a maximum error of 100 ms may be expected which can have a difference in temperature measurements up to 11.4 K.

During post-processing of the high-speed images for detection of wetting front radius, the wetting front radius is derived by means of pixel selection. Pixel selection is subject to human error and a maximum of ± 0.4 mm is expected in the calculation of the wetting front radius (R_{wf}).

7 Numerical modeling and specifications

7.1 Modeling approach

To address the conjugate heat transfer problem in liquid jet quenching, a two-phase numerical model based on the Euler-Euler framework is developed in ANSYS Fluent 19.2. The liquid water (primary phase) is modeled as a continuous phase and the water vapor as a dispersed (secondary) phase. The bubble crowd boiling model which is previously developed in a 2D domain is adopted from Refs. [17–20] and extended to the

Table 3 Sink and source terms for evaporation

Evapora-tion $[\dot{m} < 0]$	Liquid phase [l]	Vapor phase [v]
Energy	$S_{energy,l} = -\alpha_l \cdot \rho_l \cdot C_{p,l} \frac{(T_l - T_{sat})}{\Delta t}$	$S_{energy,v} = -\dot{m} \cdot C_{p,v}(T_{sat} - T_v)$
Mass	$S_{mass,l} = \frac{S_{energy,l}}{h_v} = \dot{m}$	$S_{mass,v} = -S_{mass,l} = -\dot{m}$
Momentum	$S_{momentum,l} = \dot{m} \cdot u_l$	$S_{momentum,v} = \dot{m} \cdot u_v$

3D domain. The interaction between the phases such as evaporation and condensation phenomena are modeled by means of UDF functions by modifying the source and sink terms of the conservation equations for mass, momentum and energy represented in Eqs. (8–10). Here, "m" refers to the liquid (l) or vapor phase (v), "i, j" are the vector indices and "α" is the volume fraction respectively.

$$\frac{\partial}{\partial t}(\alpha_m \rho_m) + \frac{\partial}{\partial x_i}(\alpha_m \rho_m u_i) = S_{mass} \tag{8}$$

$$\frac{\partial}{\partial t}(\alpha_m \rho_m u_i) + \frac{\partial}{\partial x_j}(\alpha_m \rho_m u_i u_j) = -\alpha_m \frac{\partial p}{\partial x_i} + \frac{\partial}{\partial x_j}(\alpha_m \tau_{ij}) + \alpha_m \rho_m g_i + S_{momentum} \tag{9}$$

$$\frac{\partial}{\partial t}(\alpha_m \rho_m h_m) + \frac{\partial}{\partial x_i}(\alpha_m \rho_m u_i h_m) = -\alpha_m \frac{\partial(p u_i)}{\partial x_i} + \frac{\partial}{\partial x_j}(\alpha_m \tau_{ij} u_i)$$
$$- \alpha_m \frac{\partial \dot{q}_i}{\partial x_i} + \alpha_m \rho_m g_i u_i + S_{energy} \tag{10}$$

In this computational approach, the evaporation and condensation within each computational cell is determined based on a heat flux check compared with the critical heat flux (Eq. 11) [17, 18, 20].

$$\dot{q}_{crit} = -\alpha_l \cdot \rho_l \cdot C_{p,l} \frac{(T_v - T_{sat})}{\Delta t} \tag{11}$$

The sink and source terms for the evaporation are presented in Table 3. Similarly, the terms for the condensation can be derived. Since an Euler-Euler approach is applied, the liquid/vapor interface can be smeared over some computational cells, however satisfactory results are produced by providing sufficient cell refinement.

In comparison to a classical VOF approach the required number of computational cells for proper film resolution are reduced by implementing the Euler-Euler approach. The identification of the interface as well as the active boiling regimes can be accomplished with the help of

Table 4 Boiling regimes based on the vapor volume fraction

Vapor volume fraction [α_v]	Boiling regime
$\alpha_v \to 0$	Pure convection
$0 < \alpha_v < 1$	Transition/nucleate boiling
$\alpha_v \to 1$	Film boiling

vapor volume fraction (α_v) as in Table 4. The secondary phase (water vapor) in the bubble crowd model is considered as an assembly of vapor bubbles, in which the bubble diameter is modeled (Eq. 12) dependent on the vapor volume fraction (α_v), based on experimental results [35–40]. The model parameters and the under relaxations adopted are concluded in Table 5. The standard under relaxations are generally applied but in order to attain convergence some under relaxation factors are reduced as derived in [19, 20]. The k-ω SST turbulence model is implemented as this provides the best combination for the near wall flow as well as the flow away from the wall [41]. The y+ value for the grid close to the wall is maintained to y+ < 1 by providing the required cell height.

$$d_v[mm] = (0.5 \cdot \alpha_v) + 0.1 \tag{12}$$

Table 5 Model parameters and under relaxations for the simulation

Parameter	Applied model/value
Turbulence	k-ω SST Mixture model
Heat transfer (Phases)	Ranz Marshall
Surface Tension	Continuum surface force
Drag	Universal drag
PV Scheme	Coupled
Spatial discretization	Green Gauss node based
Pressure	Second order
Momentum	Second order upwind
Volume fraction	QUICK Scheme
Turbulent kinetic energy	Second order upwind
Turbulent dissipation rate	Second order upwind
Energy	Second order upwind
Flow courant number	1
U-R Momentum	0.55
U-R Pressure	0.55
U-R Density	0.65
U-R Body forces	1
U-R Volume fraction	0.1
U-R Turbulent kinetic energy	0.95
U-R Specific dissipation rate	0.95
U-R Turbulent viscosity	0.4
U-R Energy	0.5
Time step	5×10^{-4} s

Table 6 Boundary conditions for simulations

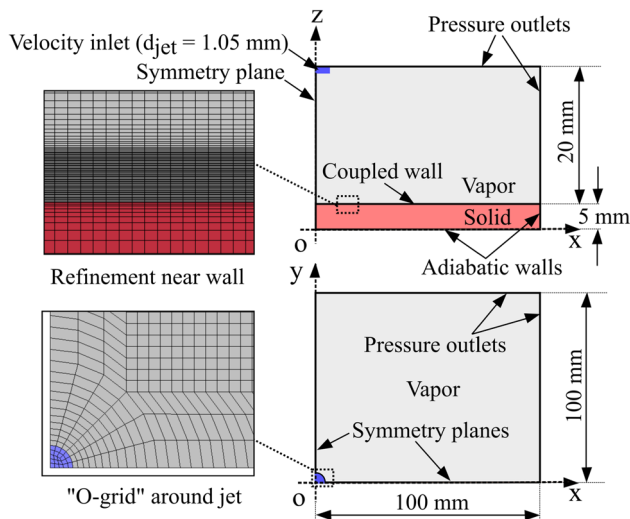| Parameter	Al-alloy	St-steel
$T_{p,o}$	773.15 K (500 ℃)	903.15 K (630 ℃)
T_{water}	292.15 K (19 ℃)	292.15 K (19 ℃)
V_{jet}	15, 20, 25 m/s	17.7 m/s
Re_{jet}	15690, 20920, 26150	18514
d_{jet}	1.05 mm	1.05 mm

The numerical cases simulated in this study demand high computing power and memory. Therefore, these simulations are performed with the help of HLRN/NHR facility (North-German Super Computing Alliance) [42]. Furthermore, the study cases are only simulated up to a maximum flow time of t < 3.5 s.

The validation cases with the Al-alloy and the St-steel are simulated with the boundary conditions listed in Table 2 (Section 3). Further simulation analysis and the variations are calculated with the boundary conditions as mentioned in Table 6.

7.2 Computational domain

The computational domain and the spatial discretization are created with ANSYS ICEM-CFD 19.2. A domain sketch with the boundary conditions and the computational mesh are shown in Fig. 17.

As the single jet quenching process is symmetric around the jet axis, one quadrant of the full domain is created for the simulation. The water jet is modeled as velocity inlet and the surroundings as pressure outlets. The wall between room (fluid) and solid is implemented as a coupled wall.

The remaining walls are modeled as adiabatic. The mesh is generated with blocked mesh feature and an "O-grid" is created around the circular water jet. Since hexahedral cells are generated, this helps to reduce the total number of computing cells significantly compared to tetrahedral cells. The region near to the wall up to height above the plate of 1.1 mm is refined where the water film flow occurs. Four different meshes are created where the cell height in this refined region is varied. The overall minimum quality of the mesh is 0.57 [> 0.3] and the minimum angle of 47.5° [> 18°] [43, 44].

7.3 Mesh study and validation of the numerical model

For investigating the influence of the mesh, a mesh study has been carried out with the following meshes with different cell heights near the wall/fluid region such as coarse (120 μm), medium (57 μm), fine (35 μm) and very fine (20 μm) for the simulation of validation case with Al-alloy (Table 2). These meshes have total computational cells of 4.7×10^6, 5.6×10^6, 6.0×10^6 and 6.9×10^6 respectively.

In Fig. 18, the impinging surface temperature along the plate radius (r) at time instant t = 0.5 s from different meshes are presented. The figure shows that the results are quite mesh dependent and the wetting front propagation is significantly affected by the cell height (wall/fluid) as already observed in a previous study [18]. For this reason, the very fine mesh is selected for the further investigation in order to obtain reasonably mesh independent results to be verified by experiments. A further reduction of the cell height is not


Fig. 17 Computational domain and mesh generated for simulation
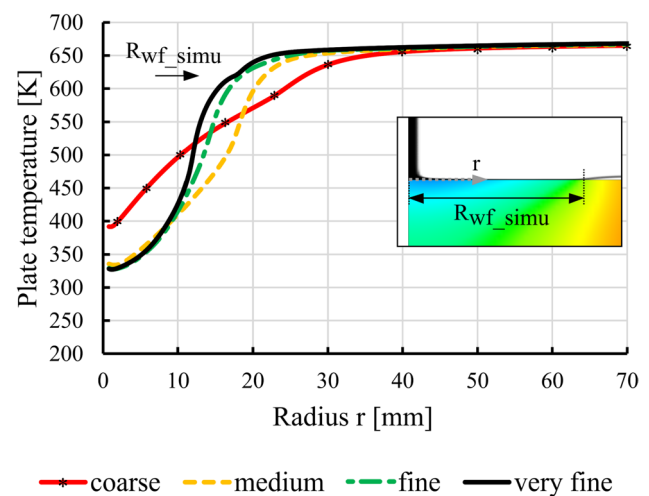
Fig. 18 Mesh study, plate impinging surface temperature from Al-alloy quenching (validation case) at time t = 0.5 s
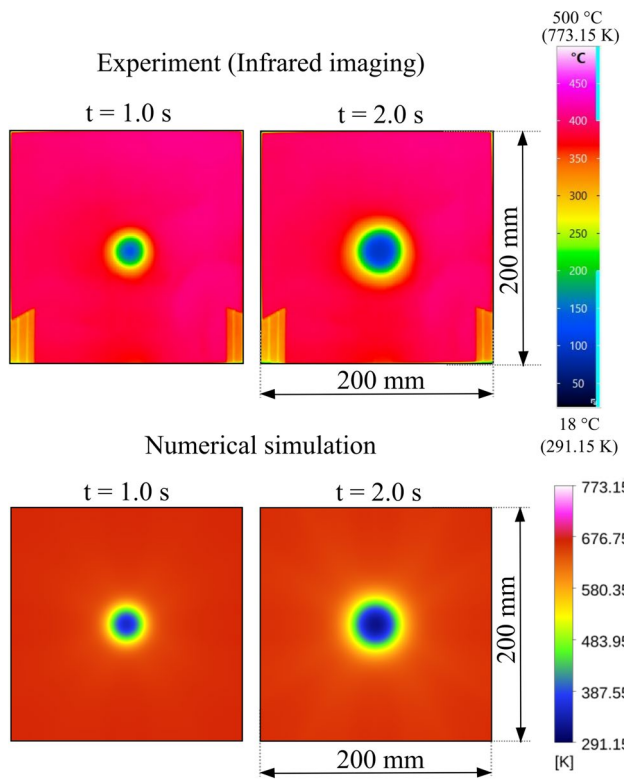
Fig. 19 Qualitative validation, non-impinging surface temperature at t = 1.0 and 2.0 s from Al-alloy quenching (validation case)

considered as the computational effort will be too high along with the complexity of the transient data storage.

The numerical model is validated qualitatively and quantitatively. The validations based on the hydrodynamic and thermodynamic perspective are adopted for evaluating the strength and reliability of the numerical model. To accomplish the qualitative validation, the temperature contours at the plate non-impinging surface during the Al-alloy
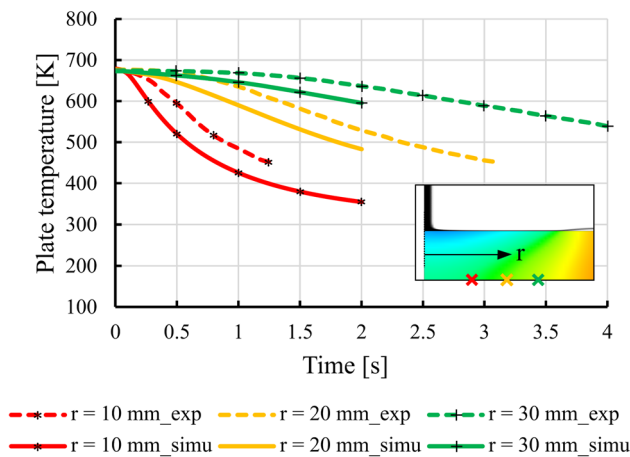
quenching (validation case) from the simulation and experiment are compared as depicted in Fig. 19. Here, a similar cold and hot zone propagation can be observed. However, the numerical results show a slightly faster cold zone propagation may be due to the absence of the initial wetting delay (Section 6.1). Also, the water jet in the simulation is taken as coherent, but this may not be the case in experiment (i.e., due to turbulence), resulting in faster propagation in the numerical simulation.

To perform a quantitative validation (thermodynamic/transient) the numerical cooling curves at the plate non-impinging surface at certain radial distances (r) are compared with the experimental results (within the calibration range) in Fig. 20. The numerical simulation shows similar trends to the experiment. However, a faster cooling in the simulation is observed as discussed earlier. The maximum deviation is 12 % at r = 10 mm and 8 % for other positions.

To evaluate the local effects in the process quantitively, the simulated temperature over the plate length (thermodynamic/stationary) is compared with the experimental results (within calibration range) in Fig. 21. The numerical results are in good agreement with the experiments and a deviation of 10 % is observed.

To validate the hydrodynamic behavior of the numerical model, the time evolution of the wetting front is compared with experiment (Fig. 22). It is seen that the wetting front radius increases with time. But the simulation is observed to be faster than the experiment as observed earlier with the bubble crowd boiling model simulations [4, 18–20, 45, 46]. The simulated wetting front radius is on an average 3.8 mm larger than in the experiment. The deviation may be due to the wetting front initiation delay, that is not present in the simulation.

To substantiate the strength and the versatility of the numerical model as well as the model behavior at different
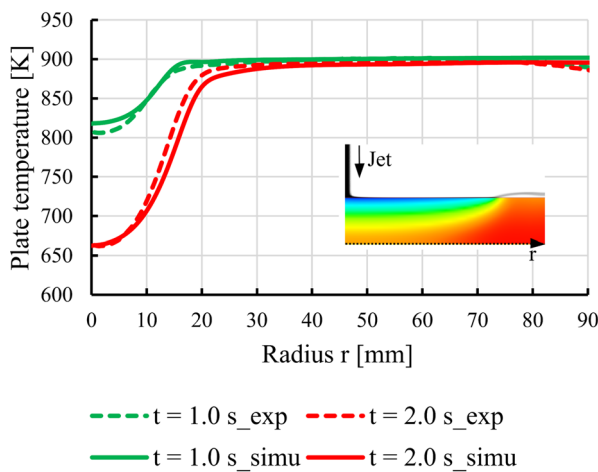

Fig. 20 Quantitative validation, plate non-impinging surface temperature with time at different radial positions (r = 10, 20 and 30 mm) for the Al-alloy quenching (validation case)
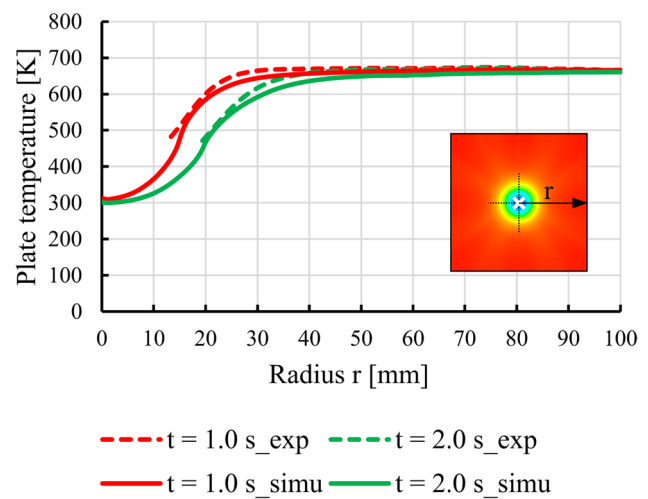
Fig. 21 Quantitative validation, plate non-impinging surface temperature across plate length at different time (t = 1.0, 2.0 s) for Al-alloy quenching (validation case)
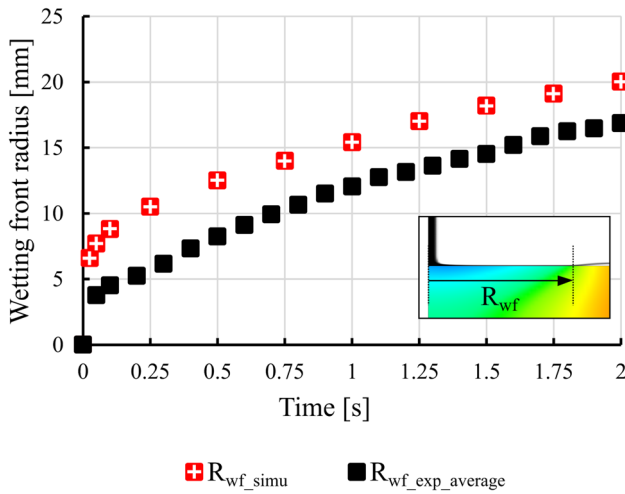
Fig. 22 Quantitative validation, wetting front propagation from simulation and experiment with time for Al-alloy quenching (validation case)

initial plate temperatures, an additional investigation with St-steel plate is performed (Tables 2 and 6). The non-impinging surface temperature along the plate length at different time instants t = 1.0 and 2.0 s during the St-steel plate quenching from the simulation and experiment (within the calibration range) is presented in Fig. 23. Simulation and experiment possess similar trends and a good agreement is observed with a deviation of less than 4 %. This implies that the model is capable of reliably investigate different plate materials and initial temperatures.

From the above results, the numerical model is sufficiently validated with qualitative and quantitative approaches in which the hydrodynamic and thermodynamic perspectives are verified.

Fig. 23 Quantitative validation, non-impinging surface temperature over plate length from simulation and experiment at different time instants for St-steel plate quenching (validation case)
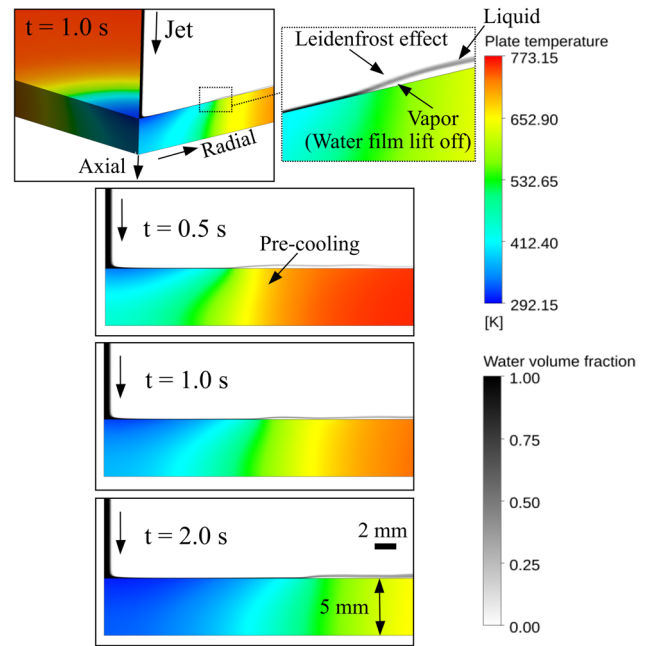
Fig. 24 Temperature and volume fraction contours for Al-alloy quenching with $T_{p,o} = 773.15$ K and $V_{jet} = 20$ m/s

8 Discussion of numerical results

8.1 Plate temperature and volume fraction contours

Figure 24 depicts the spatial and temporal temperature evolution as well as the volume fraction contours from the Al-alloy plate quenching with $T_{p,o} = 773.15$ K (500 ℃) and $V_{jet} = 20$ m/s. The axial and the radial heat transfer with respect to the jet axis is observed which is increasing with time as the cold zone propagates. Moreover, the Leidenfrost effect is directly visible from the results, where the water film lifts off from the hot surface. The wetting front radius is seen to qualitatively increase with time as the wetting front position moves to the right. A pre-cooling of the hot zone can be seen from the results.

8.2 Plate temperature and gradient

The local plate temperature for different time instants at the non-impinging surface during the Al-alloy quenching is shown in Fig. 25. It is seen that the axial and radial heat transfer increases with time. The precooling of the hot area is observed to increase with time.

Similarly, in Fig. 26 the plate impinging surface temperature for Al-alloy quenching with $T_{p,o} = 773.15$ K and $V_{jet} = 20$ m/s at different time instants is shown. As seen earlier the axial and radial heat transfer increases with time as well as the pre-cooling by conduction towards the hot outer region grows.
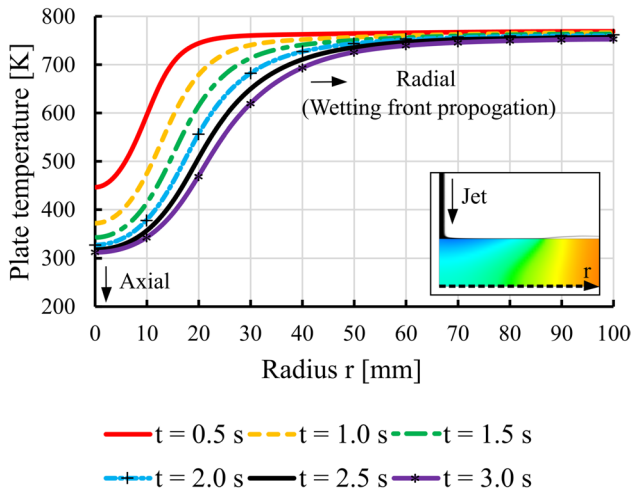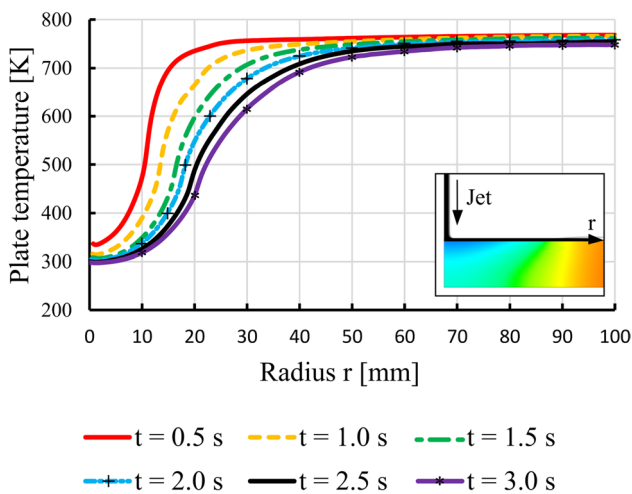
Fig. 25 Plate non-imping surface temperature at different time instants for Al-alloy quenching with $T_{p,o} = 773.15$ K and $V_{jet} = 20$ m/s
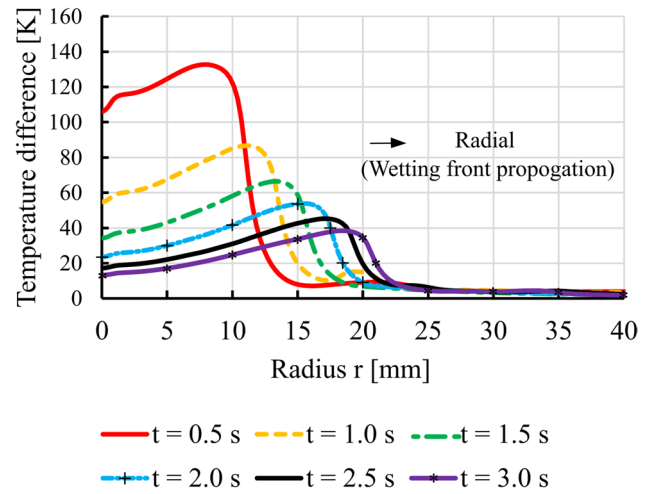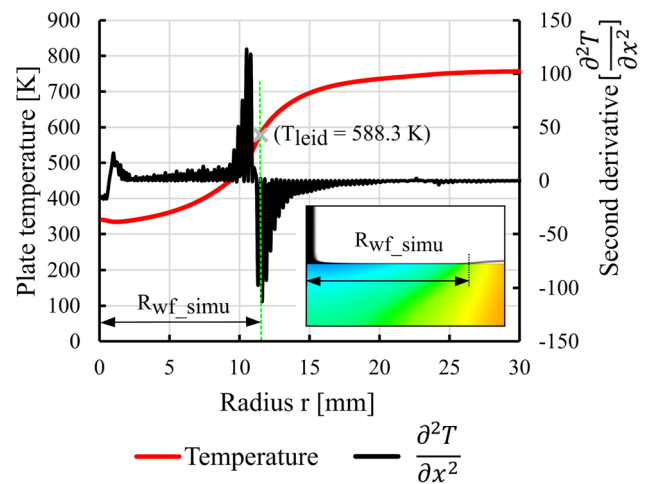

Fig. 27 Temperature difference across the plate impinging and non-impinging surface temperature for Al-alloy quenching with $T_{p,o} = 773.15$ K and $V_{jet} = 20$ m/s

However, compared to the plate non-imping surface temperature, the temperature curves from the impinging surface exhibit a significantly higher slope due to the intensive cooling occurring at the hot surface. Therefore, the temperature gradient between the impinging and non-impinging surface are calculated and illustrated in Fig. 27. It is seen that during the start, higher temperature gradients occur, which decrease over time. These gradients result in severe thermal stresses leading to material deformation and cracking.

8.3 Computing T_{leid}, R_{wf} and boiling zones

The determination of the Leidenfrost temperature (T_{leid}) and the wetting front position (R_{wf}) are calculated from the minimum of the second derivative of the surface

temperature at the impinging side over space/time [14, 18, 47]. Figure 28 shows the method with the impinging surface temperature at $t = 0.5$ s for the Al-alloy quenching, resulting in $T_{leid} = 588.3$ K (315.2 °C) and a wetting front radius $R_{wf\_simu} = 11.6$ mm.

In flow boiling processes, the maximum heat flux temperature (T_{MHF}) and the corresponding radial position (R_{MHF}) are of interest. These values can be calculated by superimposing the heat flux curve with the impinging surface temperature as shown in Fig. 29. This procedure provides a maximum heat flux temperature $T_{MHF} = 494.4$ K (221.3 °C) and $R_{MHF} = 10.4$ mm, which is less than the corresponding $R_{wf} = 11.6$ mm (Fig. 28). It should be noted that the boiling width from the maximum heat flux point to the wetting front

Fig. 26 Plate impinging surface temperature at different time instants from Al-alloy quenching with $T_{p,o} = 773.15$ K and $V_{jet} = 20$ m/s


Fig. 28 Determination method for T_{leid} and R_{wf_simu} illustrated for Al-alloy quenching (validation case) with $T_{p,o} = 773.15$ K and $V_{jet} = 20$ m/s at $t = 0.5$ s
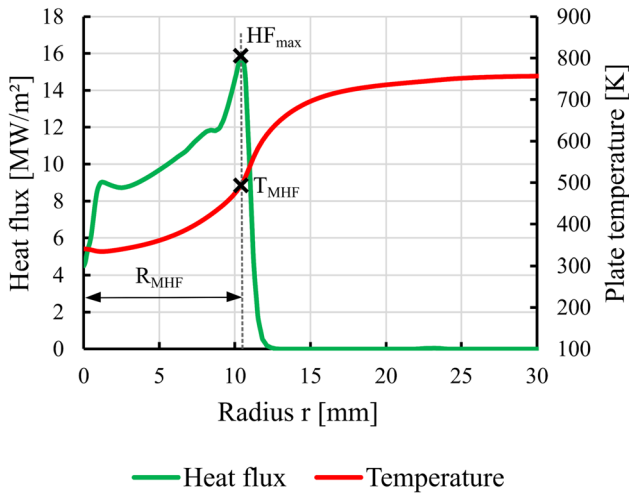
Fig. 29 Computing method for T_{MHF} and R_{MHF} for Al-alloy quenching with $T_{p,o} = 773.15$ K and $V_{jet} = 20$ m/s at t = 0.5 s

position is approximately 1.2 mm. In [18] for steel plate quenching it has been observed in between 0.5 to 2 mm as f(Re$_{jet}$) for $d_{jet} = 1.05$ mm. An increased heat flux is observed close to the jet axis, because the quenching at this location (stagnation point) occurs at increased pressure as observed for the stationary plate quenching [8, 10–13]. Close to the jet axis the viscous and the thermal boundary layer thickness are minimum [48, 49] as well as fresh water at lower temperature is in contact (at stagnation zone) which leads to an intensive cooling action.

From the above results, the single jet plate quenching can be divided into 4 zones (like Nukiyama curve) as shown in Fig. 30. For Al-alloy quenching with $T_{p,o} = 773.15$ K and $V_{jet} = 20$ m/s at t = 0.5 s. **Zone 1** (Film boiling) is the region at $T_s > T_{leid}$, in this region there is no wetting and the water
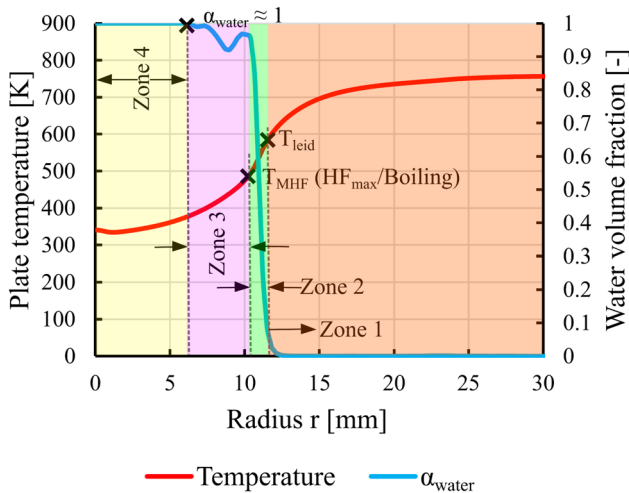
film lifts off from the hot surface resulting in a poor heat transfer regime. Large temperature gradient exists at the end of this zone. In this region $\alpha_{water} = 0$, which means it is completely filled with vapor. **Zone 2** (Transient boiling) is the region where $T_{leid} < T_s < T_{MHF}$ (HF$_{max}$). Here wetting is reestablished, however, due to the higher surface temperature, wetting and non-wetting co-exist in this region. The heat flux increases and reaches a maximum value at the end of this zone where a steep slope in the temperature curve can be observed. Thereafter, **Zone 3** (Nucleate boiling) emerges, in this zone the surface temperature further decreases with a lower slope than in zone 2, the heat flux and heat transfer comparably reduce and at the end of the zone the vapor bubble generation drops. In this zone, α_{water} approaches to higher value where slower bubble generation is expected. Finally, the **Zone 4** (pure convective heat transfer) is reached in which the surface temperature falls below the boiling temperature and there exist only pure convective heat transfer, here in the near wall region $\alpha_{water} \approx 1$ is attained. However, in case of a jet quenching, this region may have an appreciably higher transfer due to pressure in the stagnation zone, lower thickness of the viscous and the thermal boundary layers.

8.4 Heat flux and HTC

The distribution of the maximum heat flux (HF$_{max}$) and the maximum heat flux position (R$_{MHF}$) with time for Al-alloy quenching with $T_p = 773.15$ K and $V_{jet} = 20$ m/s is presented in Fig. 31. Here, HF$_{max}$ decreases with time and the position moves radially outwards. Across the radial position, the fluid flow velocity decreases and therefore HF$_{max}$ decreases accordingly. A similar trend has been observed for

Fig. 30 Boiling zones in relation to the Nukiyama curve (Fig. 5(a, b)) for Al-alloy quenching with $T_{p,o} = 773.15$ K and $V_{jet} = 20$ m /s at t = 0.5 s
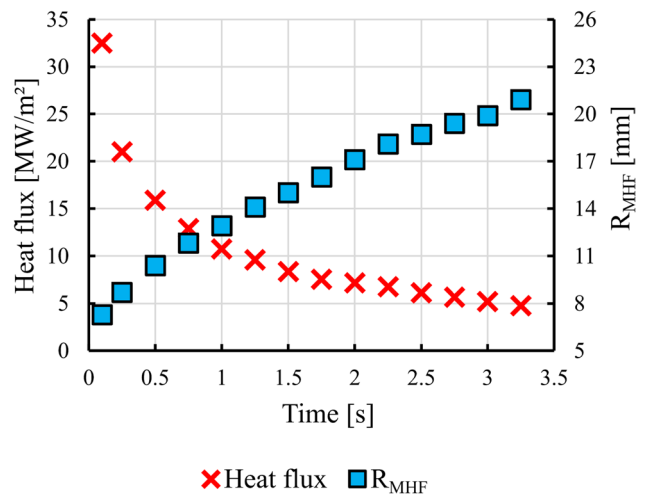
Fig. 31 HF$_{max}$ and R$_{MHF}$ with time from Al-alloy quenching with $T_{p,o} = 773.15$ K and $V_{jet} = 20$ m/s

■ r = 10 mm   ▲ r = 15 mm
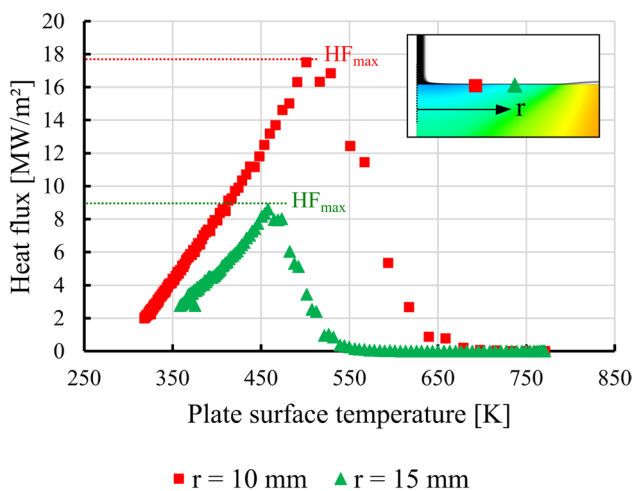
Fig. 32 Heat flux over surface temperature at different radial positions (r = 15 and 20 mm) for Al-alloy quenching with $T_{p,o} = 773.15$ K and $V_{jet} = 20$ m/s

✖ HTC$_{max\_Twater}$ ◇ HTC$_{max\_Tboi}$ ▲ HTC$_{max\_Twater\_film\_avg}$

Fig. 33 HTC$_{max}$ based on different approaches with time for Al-alloy quenching with $T_{p,o} = 773.15$ K and $V_{jet} = 20$ m/s

jet quenching of stationary plates in Refs. [1, 8, 10, 13, 14, 50]. Over time, HF$_{max}$ shows a decreasing slope of the curve.

In Fig. 32, the total heat flux (not HF$_{max}$) from the plate at different radial positions r = 15 mm and 20 mm is presented. It can be seen that the radial position close to the jet axis has a higher heat flux and this decreases further downstream. Moreover, the heat flux is lower at higher plate surface temperatures (above T_{leid}) and once it falls below the T_{leid}, the wetting initiates as well as the heat flux increases and reaches its maximum (HF$_{max}$). Thereafter, the heat flux declines and reaches lower values towards the convective regime.

Figure 33 illustrates the maximum heat transfer coefficient HTC$_{max\_Twater}$ based on a constant water temperature, HTC$_{max\_Tboi}$ with the water boiling temperature and the HTC$_{max\_Twater\_film\_avg}$ based on the local average water film temperature (along the fluid film thickness at the maximum heat flux location). The range of the HTC obtained is comparable to [19, 22, 50] for boiling flows. The three computing methods demonstrate similar trends but different values. The HTC$_{max}$ generally decreases further downstream as the fluid film velocity decreases as observed in [50]. It can be seen that the assumption of a constant fluid temperature underpredicts the HTC$_{max}$. This means the fluid temperature must be considered well during the HTC computation in case of the jet quenching. Moreover, assuming a boiling temperature is not meaningful and it may overpredict HTC$_{max}$. In classical Nukiyama experiments, the water temperature has been controlled at boiling temperature by external heating. However, in the case of the jet quenching process the water temperature changes over radial distance as well as over the fluid film height. In this perspective, considering the average
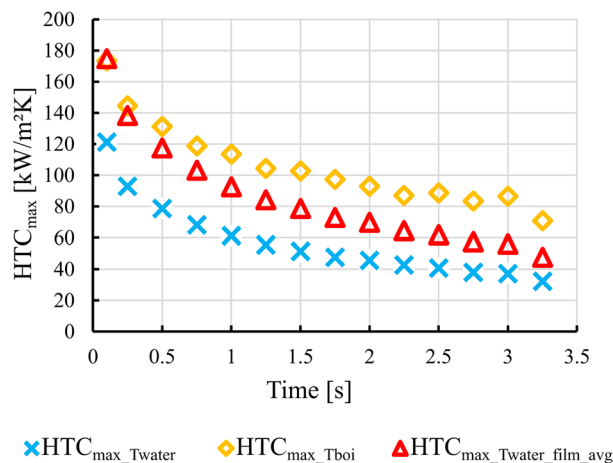
fluid film temperature along the fluid film height at HF$_{max}$ location is suggested to provide a realistic HTC$_{max}$.

As introduced in Section 4.2, the HTC can be expressed in terms of the heat flux for the two-phase flows with a power function law based on heat flux. For Al-alloy quenching (validation case) with $T_{p,o} = 773.15$ K and $V_{jet} = 20$ m/s, the HTC$_{max\_Twater\_film\_avg}$ can be correlated as shown in Eqs. 13 and Fig. 34, where values at times $0.1 < t < 3.25$ s are considered to $C = 2.06$ and $n = 0.6594$ [$R^2 = 0.989$]. In the equation, the HF$_{max}$ and HTC$_{max}$ are in W/m^2 and W/(m^2·K).

$$HTC_{max\_Twater\_film\_avg} = 2.06 \times (HF_{max})^{0.6594} \tag{13}$$
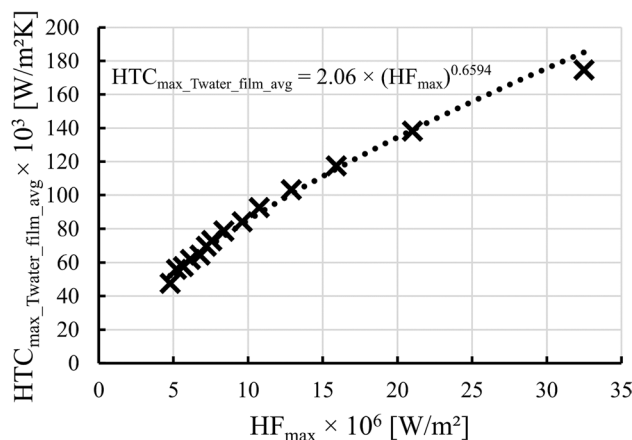
Fig. 34 Correlation for HTC$_{max\_Twater\_film\_avg}$ for Al-alloy quenching with $T_{p,o} = 773.15$ K and $V_{jet} = 20$ m/s
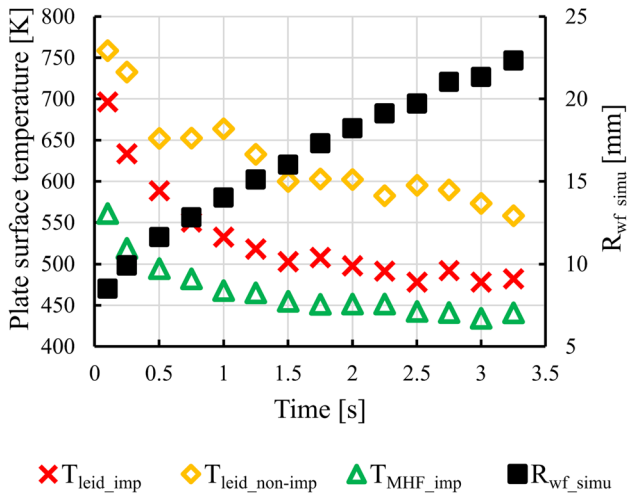
Fig. 35 Variation of T_{leid_imp}, $T_{leid\_non-imp}$, T_{MHF_imp} and R_{wf_simu} with time during Al-alloy quenching with $T_{p,o} = 773.15$ K and $V_{jet} = 20$ m/s

Fig. 36 Computing w_{pc} during Al-alloy quenching with $T_{p,o} = 773.15$ K and $V_{jet} = 20$ m/s at t = 1.0 s

8.5 Leidenfrost, MHF temperature and R_{wf_simu}

The behavior of the Leidenfrost temperature T_{leid} based on the impinging and non-impinging surface temperatures, T_{MHF_imp} and R_{wf} with time (over the radial position) for the Al-alloy quenching with $T_{p,o} = 773.15$ K and $V_{jet} = 20$ m/s is shown in Fig. 35.

The results show that T_{leid} and T_{MHF} decrease with time, initially a higher slope is seen and from a certain time the slope is very low, this means the values are converging to a constant value. It can be seen that R_{wf_simu} increases with time as the wetting front propagates radially outwards. The Leidenfrost temperature based on the impinging surface (top) and the non-impinging surface (bottom) temperatures are presented, in which the estimation from the non-impinging surface shows a higher T_{leid}. This implies that the investigation of T_{leid} based on the non-impinging surface temperature overpredicts the T_{leid} especially for the thicker plates, as high as $\Delta T = 131$ K in this case of 5 mm Al-alloy plate quenching. Therefore, the investigations based on the plate non-impinging surface (back side) may account for larger uncertainties. Thus, the evaluations in this work are further based on the impinging surface (top) properties. Initially, a higher T_{leid} is observed due to the abrupt wetting of the surface, which initiates a wetting at higher surface temperature. The Leidenfrost temperature T_{leid} decreases with time because the hot plate also cools down due to the heat transfer to the surrounding. There is also a heat transfer from the hot zone to the cold zone due to the thermal conduction in the material. A similar trend of decreasing T_{leid} over time/radius has been observed in [14, 18]. Moreover, in [14] during the quenching of a 4 mm copper plate (higher thermal conductivity) from $T_{p,o} = 773.15$ K with a full jet, the evaluations based on the non-impinging surface
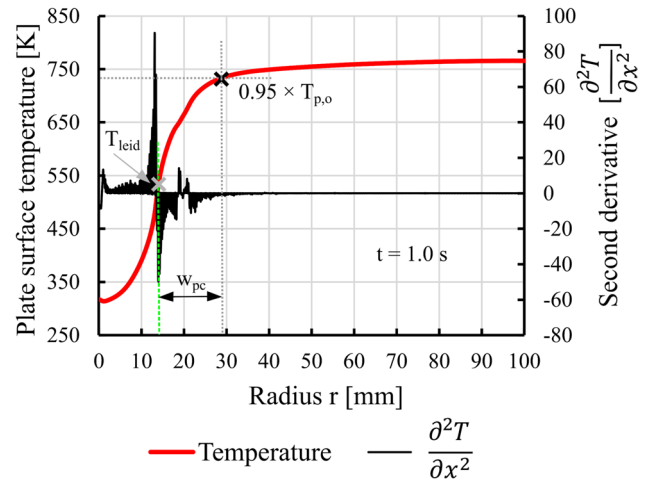
temperature showed that the T_{leid} in the range of 603–693 K as well as the T_{MHF} in the range of 473–563 K, which is confirmed with the results obtained here.
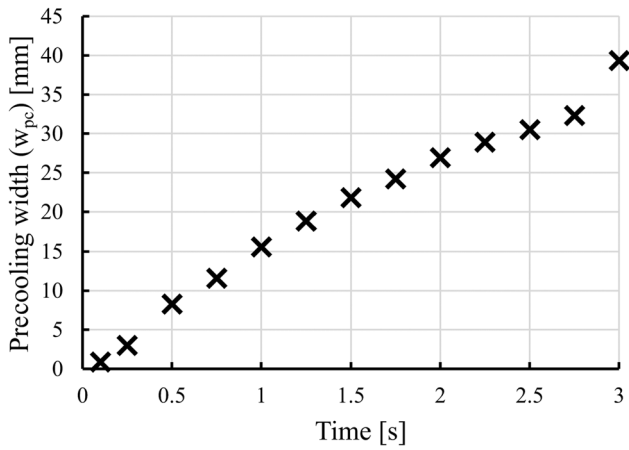
8.6 Precooling width (w_{pc})

Generally, the cooling within the wetting front is mostly focused. However, for materials with higher thermal conductivity such as Al-alloy, a precooling can occur outside the wetting front region. This should be investigated as this contributes to properly design the nozzle spacing for quenching processes with nozzle fields. Higher energy efficiency with lower water consumption can be attained by applying appropriate nozzle spacing in this process.

The precooling width (w_{pc}) is quantitatively defined to evaluate the effect. The w_{pc} is the distance between the wetting front position and the radial spatial location at which the plate surface temperature reaches 95% of the initial plate temperature ($T_{p,o}$) along the plate length (impinging/top surface) as in Fig. 36. This is described in Eq. 14 and 95 % is chosen because the surface outside the quenching area is also cooled down by the surrounding. This arbitrary assumption helps to generalise the calculation method.

$$w_{pc} = R_{simu\_95\%Tp,o} - R_{wf\_simu} \qquad (14)$$

The precooling width over time for Al-alloy quenching with $T_{p,o} = 773.15$ K and $V_{jet} = 20$ m/s is shown in Fig. 37. The w_{pc} increases with time, this means the heat transfer from the non-wetted hot zone towards the wetted cold zone is accelerated with time as the wetting front radially propagates. The higher precooling width with time indicates that the regions outside the wetting front are indirectly cooled. The nozzle spacing can also be further determined considering w_{pc}, so that larger cooling
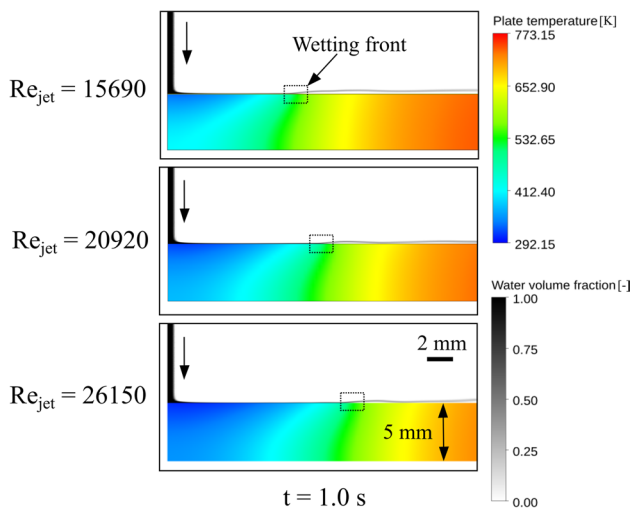
Fig. 37 Precooling width w_{pc} over time for Al-alloy quenching with $T_{p,o} = 773.15$ K and $V_{jet} = 20$ m/s
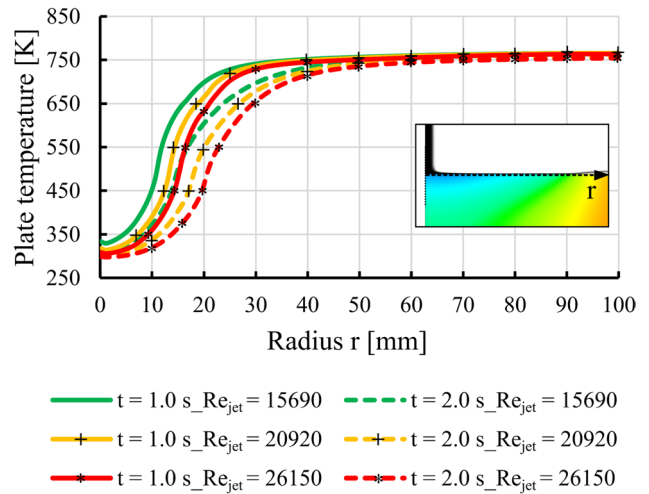
areas can be attained with a minimum number of nozzles, thereby reducing the water consumption and the energy for water pumping. A large precooling width implies that the distance between the nozzles in an array of nozzles may be increased by which a better process efficiency can be attained.

8.7 Influence of jet Reynolds number (Re_{jet})

In order to investigate the influence of the jet Reynolds number (Re_{jet}) on the heat transfer, simulations are carried out for the Al-alloy plate, where $T_{p,o} = 773.15$ K and the jet Reynolds number Re_{jet} is varied such as $Re_{jet} = 15690$, 20920 and 26150 ($V_{jet} = 15$, 20 and 25 m/s) (Table 6).

Fig. 39 Surface temperature across the plate length with time for Al-alloy plate quenching with $T_{p,o} = 773.15$ K and varying Re_{jet}

Figure 38 presents the temperature and volume fraction contours for Al-alloy jet quenching at $t = 1.0$ s. The results show that the cooling is faster with increasing Re_{jet}, where the axial and radial heat transfer increases due to the increased fluid film velocity. The wetting front radius is also seen to be increasing with Re_{jet}. The higher fluid film velocity can expel the vapor generated at the periphery of the wetting front.

In Fig. 39, the surface temperature over the plate length for varying Re_{jet} at two-time instants $t = 1.0$ and 2.0 s are compared. As Re_{jet} increases, the curves are observed to be wider which means the wetting front is larger, this implies a faster cooling action.

The influence of Re_{jet} on the temperature difference from top to bottom surface and the wetting front radius is
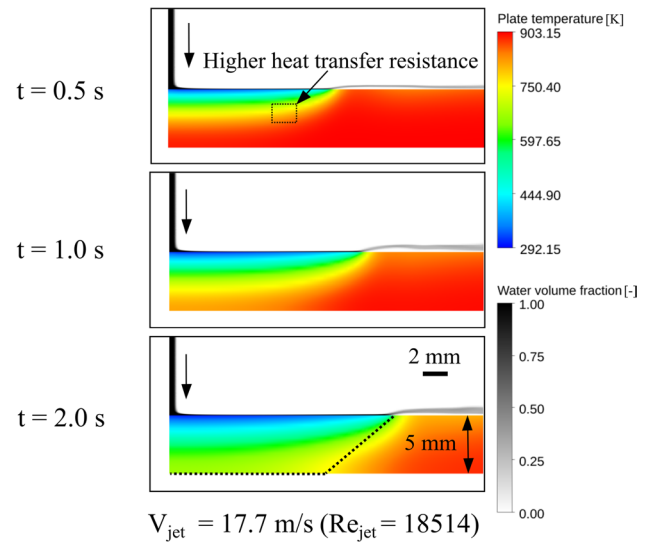

Fig. 38 Temperature and volume fraction contours for Al-alloy plate quenching with $T_{p,o} = 773.15$ K and varying Re_{jet}
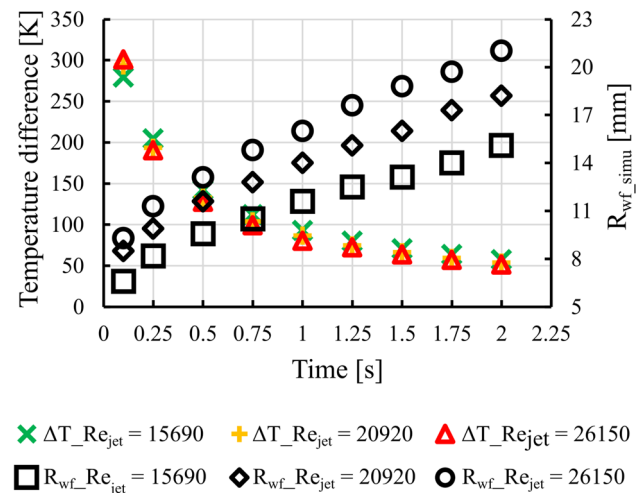
Fig. 40 Influence of Re_{jet} variation on temperature gradient and wetting front radius for 5 mm Al-alloy quenching with $T_{p,o} = 773.15$ K
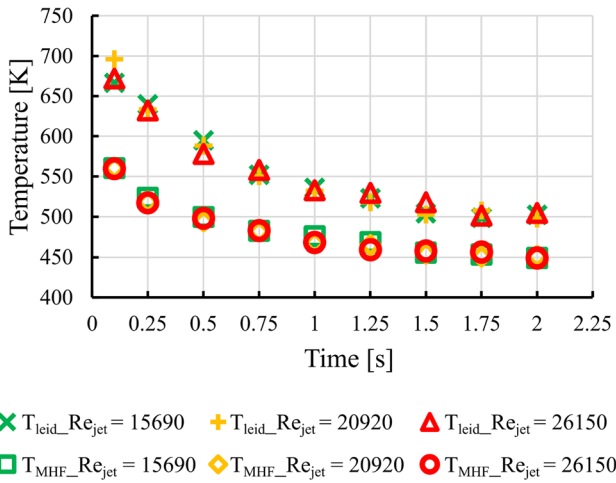
Fig. 41 Influence of Re_{jet} on T_{leid} and T_{MHF} for Al-alloy quenching with $T_{p,o} = 773.15$ K

shown in Fig. 40. In general, the temperature difference decreases with time, where only minor influence is observed with Re_{jet} variation considered in this analysis. The wetting front radius increases with increasing Re_{jet}. Here, with increased Re_{jet}, more volume of water per area per time is supplied and the fluid film velocity increases with Re_{jet}, forcing the vapor to drive away quickly as well as the heat transfer within the cold zone increases. In addition, as the volume of water supplied per unit area per time increases, the overall water temperature in the fluid film decreases, thereby creating a subcooling effect at the periphery of the wetting front for higher Re_{jet}. This means that the formation and crowding of bubbles may be delayed and result in larger R_{wf} as also observed in [12, 18]. The wetting front radius for 5 mm thick Al-alloy with $T_p = 773.15$ K can be related by using a power law function with Re_{jet} and time as in Eq. 15

Fig. 42 Influence of Re_{jet} on HF_{max} and w_{pc} for Al-alloy plate quenching with $T_{p,o} = 773.15$ K

$$V_{jet} = 17.7 \text{ m/s} \ (Re_{jet} = 18514)$$

Fig. 43 Temperature and volume fraction contours for St-steel plate quenching with $T_{p,o} = 903.15$ K and $V_{jet} = 17.7$ m/s
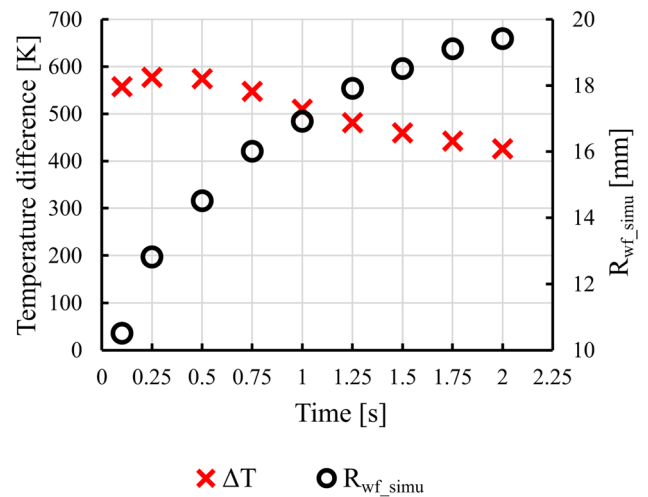
(maximum deviation < 9 %), where $15690 < Re_{jet} < 26150$ and $0.1 < t < 2.0$ s.

$$R_{wf\_simu} = 0.021 \times t^{0.28} \times (Re_{jet})^{0.66} \qquad (15)$$
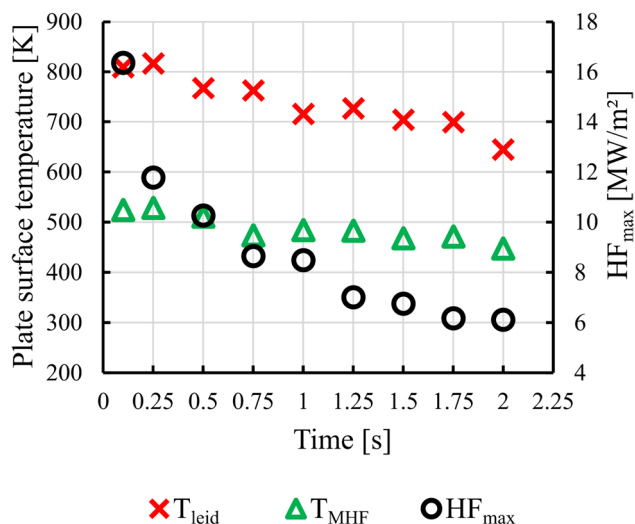
The influence of the Re_{jet} variation over T_{leid} and T_{MHF} is investigated and concluded in Fig. 41. The Leidenfrost temperature T_{leid} is higher during the beginning and later with time it slowly decreases. This behavior is due to the abrupt wetting during the start and in course of time, there is heat transfer from the hot to the cold region due to the material thermal conductivition. From a certain time, only a minor decrease is observed and T_{leid} converges. A similar trend is also seen for maximum heat flux temperature T_{MHF}. The

Fig. 44 Temperature gradient and wetting front radius with time for St-steel quenching with $T_{p,o} = 903.15$ K and $V_{jet} = 17.7$ m/s

Fig. 45 T_{leid}, T_{MHF} and HF_{max} over time for St-steel quenching with $T_{p,o} = 903.15$ K and $V_{jet} = 17.7$ m/s

Re_{jet} variation does not influence T_{leid} and T_{MHF} significantly as also observed within jet quenching in [14, 18].

The influence of the jet Reynolds number Re_{jet} variation on HF_{max} and w_{pc} over time are analysed in Fig. 42. The HF_{max} over time is not much influenced from the Re_{jet} variation considered in this study. The precooling zone width w_{pc} also remains unaffected by the Re_{jet} variation considered in this study. However, for the higher Re_{jet} case at a later time, the w_{pc} increases slightly. This could be due to the precooling effect and the intense cold zone from the higher Re_{jet}.

8.8 Influence of plate material

The influence of the plate material on the heat transfer process is analysed, for which the St-steel plate quenching (Table 6) with $T_{p,o} = 903.15$ K and $V_{jet} = 17.7$ m/s is considered. Figure 43 illustrates the temperature and volume fraction contours at different time instants. While comparing this behavior with Fig. 24 (Al-alloy), a higher heat transfer resistance can be seen within St-steel quenching. This is due to the lower thermal conductivity of the St-steel material and a sharp transition between the hot and the cold zones exist which can lead to a high temperature gradient within the material. The wetting front radius increases with time and propagates radially outwards. In contrast to the Al-alloy, it can be observed that the plate contact surface below the water film has an intensive cold region, where the increase of the surface temperature just below the water film is much slower for St-steel. Therefore, compared with higher conductive materials, St-steel may have a lower surface temperature during quenching, resulting in a relative lower heat flux and HTC. Moreover, from Fig. 43 a larger

cold zone radius is seen at the impinging side and smaller over the non-impinging surface (dashed lines, t = 2.0 s). This implies that the evaluation of the process directly from the non-impinging surface details especially for thick plates with lower thermal conductivity may have a higher degree of uncertainty such as R_{wf}, T_{leid} etc.

The temperature gradient (ΔT) and the wetting front radius R_{wf_simu} with time for the St-steel quenching are shown in Fig. 44. As in the case for Al-alloy, the R_{wf} increases with time. But a high temperature gradient exists for the St-steel quenching which can give rise to larger material distortion. The behavior of T_{leid}, T_{MHF} and HF_{max} for the St-steel quenching is illustrated in Fig. 45. The Leidenfrost temperature T_{leid} decreases very slowly in case of the St-steel in contrast to the Al-alloy, a similar trend is also seen for T_{MHF}. In [18], during steel plate quenching from $T_{p,o} = 973.15$ K, the T_{leid} resides within the range of 673–873 K which is also in the range to the results obtained.

Higher HF_{max} can be seen during the start and this decays with time. However, while comparing the HF_{max} from the Al-alloy (Fig. 31), even though the St-steel simulation has been performed with a higher initial plate temperature $T_{p,o} = 903.15$ K than the Al-alloy ($T_{p,o} = 773.15$ K), a comparably lower HF_{max} is obtained for St-steel. This is attributed to the reason that the St-steel plate has very high heat transfer resistance and the surface temperature is lower and not quickly reheated as in Al-alloy. It is observed that a higher thermal conductive material can result in higher heat flux [51–53].

9 Conclusion

A two-phase flow boiling model for quenching processes has been developed in the 3D domain and sufficiently validated, considering the hydrodynamic and thermodynamic aspects as well as for different plate materials and initial temperatures.

A detailed investigation has been carried out for the jet quenching with the plate material Al-alloy. The radial positions close to the jet axis are cooled down faster. The maximum heat flux (HF_{max}) as well as the HTC_{max} decreases away from the jet axis. The HTC_{max} based on the average water temperature along the water film thickness can be expressed as a power law function in terms of HF_{max}. Higher Leidenfrost temperature (T_{leid}) and maximum heat flux temperature (T_{MHF}) are observed at the beginning, which decreases with time and after a certain time onwards, only a minor change is observed. The influence of the cooling outside the wetting front is expressed quantitatively by the precooling width (w_{pc}) which is observed to increase with time.

Furthermore, the influence of the jet Reynolds number (Re_{jet}) on the heat transfer is evaluated with the material Al-alloy. With increasing Re_{jet}, the cooling intensity increases. The wetting front radius (R_{wf}) is found to increase with Re_{jet} and can be expressed by a power law function based on Re_{jet} and time t for Al-alloy plate quenching. The temperature gradient between the impinging and the non-impinging surfaces is not much influenced from the Re_{jet} variation. The T_{leid} and T_{MHF} remain unaffected by the Re_{jet} variation considered in this study.

The influence of the plate materials on the quenching process is evaluated by considering simulations with the St-steel and Al-alloy plates. A very high heat transfer resistance is observed for St-steel. The transition from the cold zone to the hot zone is sharp and large temperature gradients exist between the impinging and the non-impinging surface for the St-steel. Comparing with Al-alloy, a lower HF_{max} is observed for St-steel. The T_{leid} and T_{MHF} are decreasing with time for the St-steel, however with a lower slope than Al-alloy.

This validated numerical model can be further extended to simulate quenching processes in quite different configurations like nozzle fields, flat jets, pulsating jets and even for non-flat plates or moving plates.

Declarations

References

1. Specht E (2018) Heat and Mass Transfer in Thermoprocessing. DIV Deutscher Industrieverlag GmbH / Vulkan-Verlag GmbH, Essen, Germany

2. Fujimoto H, Shiramasa Y, Morisawa K, Hama T, Takuda H (2015) Heat Transfer Characteristics of a Pipe-laminar Jet Impinging on a Moving Hot Solid. ISIJ Int 55(9):1994–2001. https://doi.org/10.2355/isijinternational.ISIJINT-2015-124

3. Wassenberg JR, Stephan P, Gambaryan-Roisman T (2019) The influence of splattering on the development of the wall film after horizontal jet impingement onto a vertical wall. Exp Fluids 60(11). https://doi.org/10.1007/s00348-019-2810-6

4. Narayan NM, Gopalkrishna SB, Mehdi B, Ryll S, Specht E, Fritsching U (2023) Multiphase numerical modeling of boiling flow and heat transfer for liquid jet quenching of a moving metal plate. Int J Therm Sci 194(108587):1–17. https://doi.org/10.1016/j.ijthermalsci.2023.108587

5. Parsa H, Saffar-Avval M, Hajmohammadi MR, Ahmadibeni G (2023) Improvement of solar air heaters performance with PCM-filled baffles and storage bed. Int J Mech Sci 260. https://doi.org/10.1016/j.ijmecsci.2023.108629

6. Mirahsani S, Ahmadpour A, Hajmohammadi MR (2023) Optimal design of an array of porous obstacles in a partially heated channel using lattice Boltzmann method for the heat transfer enhancement. Int Commun Heat Mass Transf 143. https://doi.org/10.1016/j.icheatmasstransfer.2023.106737

7. Hajmohammadi MR, Bahrami M, Ahmadian-Elmi M (2021) Thermal performance improvement of microchannel heat sinks by utilizing variable cross-section microchannels filled with porous media. Int Commun Heat Mass Transf 126. https://doi.org/10.1016/j.icheatmasstransfer.2021.105360

8. Karwa N, Stephan P (2013) Experimental investigation of free-surface jet impingement quenching process. Int J Heat Mass Transf 64:1118–1126. https://doi.org/10.1016/j.ijheatmasstransfer.2013.05.014

9. Wang H, Yu W, Cai Q (2012) Experimental study of heat transfer coefficient on hot steel plate during water jet impingement cooling. J Mater Process Technol 212(9):1825–1831. https://doi.org/10.1016/j.jmatprotec.2012.04.008

10. Hall DE, Incropera FP, Viskanta R (2001) Jet impingement boiling from a circular free surface jet during quenching: Part 1 Single phase jet. J Heat Transfer ASME 123:901–910. https://doi.org/10.1115/1.1389061

11. Robiduo H, Auracher H, Gardin P, Lebouche M (2002) Controlled cooling of a hot plate with a water jet. Exp Thermal Fluid Sci 26:123–129

12. Oliveira AVS et al (2022) Experimental study of the heat transfer of single-jet impingement cooling onto a large heated plate

near industrial conditions. Int J Heat Mass Transf 184. https://doi.org/10.1016/j.ijheatmasstransfer.2021.121998

13. Nobari AH, Prodanovic V, Militzer M (2016) Heat transfer of a stationary steel plate during water jet impingement cooling. Int J Heat Mass Transf 101:1138–1150. https://doi.org/10.1016/j.ijheatmasstransfer.2016.05.108

14. Fang Y (2019) Influence of nozzle type and configuration and surface roughness on heat transfer during metal quenching with water. Dissertation Ph.D, Der Fakultät für Verfahrens- und Systemtechnik, Otto-von-Guericke-Universität Magdeburg, Magdeburg

15. Podowski MZ, Podowski RM (2009) Mechanistic multidimensional modeling of forced convection boiling heat transfer. Sci Technol Nucl Install 2009:1–10. https://doi.org/10.1155/2009/387020

16. Wang Z, Podowski MZ (2017) Mechanistic multidimensional modeling of forced convection boiling heat transfer. Trans Am Nucl Soc

17. Stark P (2013) Prozesssimulation der Bauteil-Abschreckung in flüssigen Medien: Zur Analyse des mehrphasigen Strömungs- und Wärmetransports in Siedeprozessen. PhD Dissertation, Production Technology, University of Bremen, Germany

18. Waldeck S (2020) Untersuchung der intensiven Kühlung von heißen Oberflächen mit Wasserstrahlen. Ph.D Dissertation, Produktionstechnik, Universität Bremen, Germany

19. Waldeck S, Woche H, Specht E, Fritsching U (2018) Evaluation of heat transfer in quenching processes with impinging liquid jets. Int J Therm Sci 134:160–167. https://doi.org/10.1016/j.ijthermalsci.2018.08.001

20. Narayan NM, Moqadam SI, Ellendt N, Fritsching U (2023) Multiphase numerical modeling and investigation of heat transfer for quenching of spherical particles in liquid pool. Int J Therm Sci 186. https://doi.org/10.1016/j.ijthermalsci.2022.108016

21. Kamenicky R, Frank M, Drikakis D, Ritos K (2022) Film boiling conjugate heat transfer during immersion quenching. Energies 15(12). https://doi.org/10.3390/en15124258

22. Stephan P, Kabelac S, Kind M, Mewes D, Schaber K, Wetzel T (2019) VDI Wärmeatlas. Springer Vieweg, Berlin, Germany

23. Infrared camera, https://www.infratec.de. Accessed 16 Feb 2023

24. Black coating, https://ulfalux.com. Accessed 4 Jul 2023

25. Furnace, https://www.thermconcept.com/. Accessed 4 Jul 2023

26. Nozzle system, https://www.lechler.com/de/. Accessed 16 Feb 2023

27. ImageJ software, https://imagej.nih.gov. Accessed 25 Jan 2022

28. Infrared data post processing software, https://www.infratec.de/thermografie/thermografie-software/. Accessed 15 Mar 2023

29. Bejan A, Kraus AD (2003) Heat Transfer Hand Book. John wiley & Sons, INC., New Jersey and Canada

30. Baehr HD, Stephan P (1998) Wärme- und Stoffübertragung. Springer

31. Nukiyama S (1934) The maximum and minimum values of the heat q transmitted from metal to boiling water under atmospheric pressure. J Japan Soc Mech Eng 37:367–374

32. Thome JR (2004) Engineering data book III. Wolverine Tube Inc, Switzerland

33. Gungor KE, Winterton RHS (1986) A general correlation for flow boiling in tubes and annuli. Int J Heat Mass Transf 29(3):351–358

34. Liscic B, Tensi HM, Canale LCF, Totten GE (2010) Quenching theory and technology. CRC Press

35. Jouhara HI, Axcell BP (2002) Forced Convection Film Boiling on Spherical and Plane Geometries. Chem Eng Res Des 80(3):284–289. https://doi.org/10.1205/026387602753582060

36. Jouhara H, Axcell BP (2009) Film boiling heat transfer and vapour film collapse on spheres, cylinders and plane surfaces. Nucl Eng Des 239(10):1885–1900. https://doi.org/10.1016/j.nucengdes.2009.04.008

37. McHale JP, Garimella SV (2010) Bubble nucleation characteristics in pool boiling of a wetting liquid on smooth and rough surfaces. Int J Multiph Flow 36(4):249–260. https://doi.org/10.1016/j.ijmultiphaseflow.2009.12.004

38. Tolubinsky VI, Kostanchuk DM (1970) Vapour bubbles growth rate and heat transfer intensity at subcooled water boiling. Fourth Int Heat Transf Conf. Paris, p 5

39. Anglart H, Nylund O (1996) CFD application to prediction of void distribution in bubbly flows in rod bundles. Nucl Eng Des 163:81–98. Elsevier

40. Kolev NI (1998) Film boiling on vertical plates and spheres. Exp Thermal Fluid Sci 18:97–115

41. Kempf A (2015) Lecture manuscript for Turbulence. University of Duisburg-Essen, Germany

42. North German Supercomputing Alliance (HLRN), https://www.hlrn.de/. Accessed 23 Jan 2023

43. Inc A (2012) ANSYS ICEM CFD Tutorial manual, Canonsburg

44. Inc A (2012) ANSYS ICEM CFD User manual, Canonsburg

45. Narayan NM, Fritsching U, Gopalkrishna SB, Mehdi B, Woche H, Specht E (2021) Investigation of heat transfer in arrays of water jets, modelling/ simulation and experimental approach. European Conference on Heat Treatment (ECHT) and 2nd International Conference on Quenching and Distortion Engineering (QDE) Online Conference. B, Germany, pp 1–2

46. Mehdi B, Gopalkrishna SB, Narayan NM, Ryll S, Woche H, Specht E, Fritsching U (2021) Quenching of moving metal plates with flat sprays and single full jet nozzle. Aachener Ofenbau- und Thermoprozess-Kolloquium September. Aachen, Germany, pp 1–2

47. Filipovic J, Incropera FP, Viskanta R (1995) Rewetting temperatures and velocity in a quenching experiment. Exp Heat Transf 8(4):257–270. https://doi.org/10.1080/08916159508946505

48. Ma CF, Gan YP, Tian YC, Lei DH (1993) Liquid Jet Impingement Heat Transfer with or without Boiling. J Therm Sci 2:32–49

49. Ma CF, Zhao YH, Masuoka T, Gomi T (1996) Analytical study on impingement heat transfer with single-phase free surface circular liquid jets. J Therm Sci 4:271–277. https://doi.org/10.1007/BF02653234

50. Chen S-J, Kothari J, Tseng AA (1991) Cooling of a moving plate with an Impinging circular water jet. Exp Thermal Fluid Sci 4:343–353

51. Wells MA, Li D, Cockcroft SL (2001) Influence of surface morphology, water flow rate, and sample thermal history on the boiling-water heat transfer during direct-chill casting of commercial aluminum alloys. Metall Mater Trans B 32B:929–939

52. Sengupta J, Thomas BG, Wells MA (2005) The use of water cooling during the continuous casting of steel and aluminum alloys. Metall Mater Trans B 36A:187–204

53. Hu X et al (2021) Investigation on subcooled flow boiling heat transfer characteristics in ICE-like conditions. Open Phys 19(1):413–425. https://doi.org/10.1515/phys-2021-0052

Authors and Affiliations

Nithin Mohan Narayan[1,2] · Udo Fritsching[1,2,3]

✉ Nithin Mohan Narayan
   n.narayan@iwt.uni-bremen.de

[1] Faculty of Production Engineering, University of Bremen,
    Badgasteinerstraße.3, 28359 Bremen, Germany

[2] Leibniz Institute for Materials Engineering-IWT,
    Badgasteinerstraße.3, 28359 Bremen, Germany

[3] MAPEX Center for Materials and Processes, University
    of Bremen, Am Biologischen Garten. 2, 28359 Bremen,
    Germany